On the Impact of Phase Errors in Phase-Dependent Amplitudes of Near-Field RISs

Ke Wang, *Member, IEEE,* Chan-Tong Lam, *Senior Member, IEEE,* Benjamin K. Ng, *Senior Member, IEEE,* and Yue Liu, *Member, IEEE*

***Abstract*—This paper investigates mutual coupling between phase-dependent amplitudes (PDAs) and designed phase shifts within pixels of near-field (NF) reconfigurable intelligent surfaces (RISs) in the presence of phase errors (PEs). In contrast to existing research that treats phase shifts with errors (PSEs) and the PDAs separately, we introduce a remaining power (RP) metric to quantify the proportion of power preserved in the signals reflected by the RIS, and we prove its asymptotic convergence to theoretical values by leveraging *extended Glivenko–Cantelli theorem*. Then, the RP of signals passing through RIS pixels is jointly examined under combined phase and amplitude uncertainties. In addition, we propose four pixel reflection models to capture practical conditions, and we derive approximate polynomial upper bounds for the RP with error terms by applying *Taylor expansion*. Furthermore, based on *Friis transmission formula* and *projected aperture*, we propose a general NF channel model that incorporates the coupling between the PSEs and the PDAs. By using *Cauchy–Bunyakovsky–Schwarz inequality* and *Riemann sums*, we derive a closed-form upper bound on spectral efficiency, and the bound becomes tighter as the pixel area decreases. We reveal that as the RIS phase shifts approach the ends of their range, the RP under independent and identically distributed PEs is smaller than that under fully correlated PEs, whereas this relationship reverses when the phase shifts are near the middle of their range. Neglecting the PEs in the PDAs leads to an overestimation of the RIS performance gain, explaining the discrepancies between theoretical and measured results.**

***Index Terms*—Reconfigurable intelligent surface, near-field communication, phase-dependent amplitude, phase error**

I. Introduction

A. Background and Related Works

Reconfigurable intelligent surfaces (RISs) hold significant potential to revolutionize wireless communication technologies [2]. Traditional investigations on the RIS have predominantly concentrated on far-field scenarios [3], [4], which are suitable for long transmission distances. Recently, however, the RIS deployed in near-field (NF) environments has exhibited distinct advantages over alternative transmission enhancement methodologies [5]–[8]. Given its non-uniform spherical wave and spatial non-stationarity features [7], the NF RIS further highlights the propagation properties of electromagnetic waves by increasing the total reflective area and placing the communication transceivers in *the Fresnel region* [8], thereby improving spectral efficiency (SE), spatial resolution, and degrees of freedom for transmission [9].

It should be noted that we cannot consider every pixel of the NF RIS as identical, since each pixel possesses its unique transmission angle and distance [5]–[9]. Consequently, the hardware characteristics of each NF RIS pixel must be individually taken into account. Moreover, in practical scenarios, *phase errors (PEs)* within the RIS cannot be overlooked [10]. Previous studies [10]–[16] primarily focused on *phase shift with errors (PSEs)*, represented as $\exp(-\jmath(\phi+\Delta))$[1] where ϕ denotes an RIS pixel phase shift, Δ represents a PE random variable (RV) that follows specific distributions, $\exp(\cdot)$ is exponential function, and $\jmath \triangleq \sqrt{-1}$. Generally speaking, there are three types of practical PEs in the RIS, i.e., *quantization errors* [10], [11], [16], *imperfect channel estimations* [10], [13], and *pixel hardware failures* [14]–[17]. In particular, Badiu *et al.* [10] initially revealed that the quantization and imperfect estimation errors in the RIS are respectively characterized by uniform ($\mathcal{UF}$) and von Mises ($\mathcal{VM}$) RVs, and an RIS cascaded path is equivalent to a direct channel with Nakagami scalar fading. Zhou *et al.* in [11] analyzed spectral and energy efficiencies of the RIS with $\mathcal{UF}$ RVs, and an important finding is that the SE is constrained regardless of the pixel number becoming exceedingly large. Besides, Yang *et al.* in [16] further explored the implications of incorporating the quantization error into the RIS system, Lu *et al.* in [13] conducted a joint analysis of the RIS system's performance, taking into account the synergistic impacts of the estimation errors and channel aging. Moreover, Sun *et al.* in [14] proposed a method for detecting failed RIS pixels based on compressed sensing, Taghvaee *et al.* [15] examined the reliability problem in the RIS by introducing an error model and a general methodology for error analysis, and Wang *et al.* in [17] revealed that hardware aging effects related to operation times of the RIS are significant in practical scenarios.

Beyond the aforementioned noises exist in the PSE $\exp(-\jmath\Delta)$, however, the actual pixel reflection coefficient exhibits its own *phase-dependent amplitudes (PDAs)* [18]–[20], which can be expressed as $\beta(\phi)$ where ϕ is phase shift and $\beta(\cdot) \in (0,1]$ refers to a nonlinear function [18].

Manuscript received 25 June, 2025; revised 1 Nov, 2025; accepted 18 December, 2025. An earlier version of this paper was presented in part at *2024 IEEE 100th Vehicular Technology Conference (VTC2024-Fall)* [1]. This work was supported by the research funding of the Macao Polytechnic University, Macao SAR, China (Project No. RP/FCA-04/2025).

Ke Wang, Chan-Tong Lam, Benjamin K. Ng, and Yue Liu are all with the Faculty of Applied Sciences, Macao Polytechnic University, Macao SAR, 999078, China, e-mail: (kewang, ctlam, bng, yue.liu)@mpu.edu.mo.

[1]Given that the transceiver of the system model in this paper has a single antenna, thus ϕ and the phase of the cascaded channel cancel each other out, and the PSE is defined as $\exp(-\jmath\Delta)$ in the rest of this work.

Model	Works	Reflection Coefficient Description	Approximated Model
Perfect	[3]–[9], [26]–[28]	Complete reflection w/o the PDA, the PSE or any PEs	$1 \cdot \exp(-\jmath\phi)$
Case I	[10]–[16], [29]	Partial reflection w/ the PSE and the PDA is a constant $\beta \in (0,1]$	$\beta \cdot \exp(-\jmath\Delta)$
Case II	[17]–[20]	Partial reflection w/ the PSE and the PDA $\beta(\phi)$ is w/o any PEs	$\beta(\phi) \cdot \exp(-\jmath\Delta)$
Case III	This paper	Partial reflection w/ the PSE and the PDA $\beta(\phi)$ is w/ an single PE	$\beta(\phi+\bar{\Delta}) \cdot \exp(-\jmath\Delta)$
Case IV	This paper	Partial reflection w/ the PSE and the PDA $\beta(\phi)$ is w/ both PEs	$\beta(\phi+\bar{\Delta}+\bar{\Theta}) \cdot \exp(-\jmath(\Delta+\Theta))$

TABLE I: Comparison between this paper and its related works. Note $\beta(\cdot) \in (0,1]$ and ϕ is the designed pixel phase shift. Δ, $\bar{\Delta}$, Θ and $\bar{\Theta}$ all denote PE RVs, $\bar{\Delta} = \iota\Delta + \sqrt{1-\iota^2}\breve{\Delta}$, where $\iota \in [0,1]$ and $\breve{\Delta}$ is i.i.d. with Δ. Θ and $\bar{\Theta}$ are defined analogously.

Specifically, Abeywickrama *et al.* [18] first introduced the approximated PDA model to mimic the equivalent circuit model of the RIS pixel, and then formulated and addressed a problem of minimizing the total transmission power through a joint optimization of the transmit beamforming vectors and the RIS phase shifts. Ozturk *et al.* in [19] investigated a problem of NF localization by utilizing the RIS accounting for the presence of the PDA, and they revealed that ignoring the PDA at the receiver can lead to substantial performance degradation. Moreover, Mosleh *et al.* [20] showed the ergodic capacity limit of the RIS system with the PDA is directly dependent on the PDA and indirectly on the phase shift.

B. Motivations and Contributions

Given the background and related works mentioned above, the motivation for this paper is summarized in Table I. In particular, although many previous works have explored the impacts of the PE in the PSE on the RIS-aided system [10]–[20], there is no research on the mutual coupling of the PSE and the PDA when the PE exists. It should be emphasized that the pixel hardware is increasingly vulnerable as it incorporates sophisticated tuning, control, and sensing systems [21]. Thus, from a practical perspective, PEs may also exist in the PDA. To this end, in this paper, we consider three regimes: (i) perfect transfer of the PE from the PSE to the PDA, i.e., $\iota = 1$ in Cases III and IV in Table I; (ii) fully random pixel imperfections that induce i.i.d. noise at the PDA, i.e., $\iota = 0$ in Cases III and IV in Table I; and (iii) intermediate correlation levels with $\iota \in (0,1)$. In practice, the pixel hardware failure [14]–[17] progressively shifts the system from (i) toward (ii). Specifically, differential degradation of RIS components (e.g., varactor diodes) desynchronizes the errors between the PSE and the PDA, thereby increasing their *statistical independence*. Consequently, as the RIS behavior approaches an i.i.d. noise model, the correlation coefficient ι decreases over time and approaches 0, reflecting the emergence of random, decoupled uncertainties driven by hardware degradations [17].

It is noteworthy that the omission of the above issues may be pivotal in accounting for the disparity between theoretical analyses and hardware validations [22]–[25]. Besides, different from the existing pixel reflection models (i.e., Perfect, Cases I and II in Table I), a practical model that explicitly captures $\mathcal{UF}$ and/or $\mathcal{VM}$ uncertainties in the PSE and/or the PDA is essential for future performance analysis and algorithm design in the NF RIS-assisted system. Therefore, the focus of this work is to determine *how the PSE and the PDA, with the PE in particular, jointly affect the RIS system performance.* The contributions are summarized as follows:

- **Hardware and theoretical modeling**. We present the hardware configuration and schematic model of an RIS pixel, and investigate how key circuit parameters affect the PDA model. Closed-form lower and upper bounds for the ideal PDA without the PE are derived.
- **New metric with asymptotic guarantee**. We introduce a new metric termed the RP to quantify energy conservation after a signal passes through an RIS pixel. By leveraging *extended Glivenko–Cantelli theorem*, we rigorously prove the asymptotic convergence of the RP to its theoretical value, thereby establishing the statistical foundation for subsequent analysis.
- **Unified reflection models and polynomial bounds**. We develop four practical pixel reflection models that jointly capture phase and amplitude uncertainties. Based on *Taylor expansion*, we derive polynomial lower bounds for the RP with quantified approximation errors. As the RIS phase shifts approach the ends of their range, the RP under i.i.d. PEs becomes smaller than that under identical PEs, whereas this relationship reverses when the phase shifts are near the middle of their range.
- **New NF channel and SE analysis**. Building on *Friis transmission formula* and *proposed reflection*, we establish a general NF line-of-sight (LoS) channel model incorporating the coupling between the PDA and the PSE. A closed-form SE expression is further derived through *Cauchy–Bunyakovsky–Schwarz (CBS) inequality* and *Riemann sums*.

C. Outline, Notations, and Reproducible Research

The remainder of this paper is organized as follows. Sec. II presents the hardware structure of the RIS pixel and its schematic model, analyzes the influence of key circuit parameters on the approximated PDA model, and derives closed-form lower and upper bounds for the ideal PDA without PEs. Sec. III introduces a unified RP-based framework and four practical pixel reflection models, along with their polynomial bounds that incorporate error terms under phase and amplitude uncertainties. Sec. IV develops a general NF LoS channel model that captures the coupling between the PDA and the PSE, and provides a closed-form analysis of SE. Extensive simulation results and performance discussions are presented in Sec. V. Finally, Sec. VI concludes the paper and outlines potential directions for future research.

Notations of this paper are as follows: $|\cdot|$ denotes absolute value, $\|\cdot\|$ is l_2 norm, $[\cdot]^{\mathsf{T}}$ is transpose operation, $(p \bmod q)$ is the remainder of the division of p by q. Besides, $\sin(\cdot)$, $\cos(\cdot)$, $\arctan(\cdot)$, and $\arccos(\cdot)$ are respectively sine, cosine, inverse tangent, and inverse cosine functions. Moreover,

$\mathcal{CN}$, $\mathcal{UF}$, $\mathcal{VM}$, $\mathbb{E}\{\cdot\}$, $\mathsf{Im}(\cdot)$, and $\mathsf{Re}(\cdot)$ represent complex Gaussian distribution, uniform distribution, von Mises distribution, expectation function, imaginary and real parts of a complex number, respectively. Furthermore, $\mathsf{Cov}(\cdot,\cdot)$ and $\mathsf{Var}(\cdot)$ denote covariance and variance operators, respectively. For reproducible research, the simulation code is available at https://github.com/ken0225/On-Impact-PEs-PDAs-NF-RISs.

II. Phase-Dependent Amplitudes in RIS Pixels

In this section, we start by elucidating the hardware configuration of the RIS pixel. Henceforth, an analysis of the approximated PDA is proposed, especially for lower and upper bounds of the PDA in the absence of the PE. Note that we focus on the NF scenario; thus, the hardware of each pixel and its own cascaded channel should be analyzed separately.

A. Hardware Structure of RIS Pixels

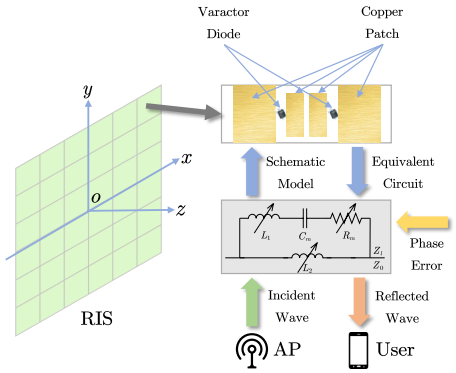

Fig. 1: Top view and equivalent circuit of the RIS pixel.

A typical RIS pixel hardware contains three layers [22], [23]. As shown in Fig. 1, the top layer contains two pairs of copper patches, each of which is connected by a varactor diode. The middle layer is a complete metallic panel, for reflecting incoming waves and preventing energy loss, and the bottom layer consists of direct current biasing lines. A single pixel can be modeled as a parallel resonant circuit [23]. Thus, without loss of generality, if an RIS has M pixels, for the m-th pixel where $m = 1, \ldots, M$, we have its equivalent impedance as [18], [23]

$$Z_m(C_m, R_m) = \frac{\jmath 2\pi f_c L_1 (\jmath 2\pi f_c L_2 + \frac{1}{\jmath 2\pi f_c C_m} + R_m)}{\jmath 2\pi f_c L_1 + (\jmath 2\pi f_c L_2 + \frac{1}{\jmath 2\pi f_c C_m} + R_m)}, \tag{1}$$

where L_1, L_2, C_m, R_m, and f_c are bottom layer inductance, top layer inductance, the m-th effective capacitance, the m-th effective resistance, and carrier frequency, respectively. If Z_0 denotes free space impedance, then the reflection coefficient of the m-th pixel can be obtained as

$$\varsigma_m = \frac{Z_m(C_m, R_m) - Z_0}{Z_m(C_m, R_m) + Z_0}. \tag{2}$$

Consequently, the final tuned phase of the m-th reflection coefficient ς_m is

$$\phi_m = \arctan\left(\frac{\mathsf{Im}(\varsigma_m)}{\mathsf{Re}(\varsigma_m)}\right). \tag{3}$$

It should be emphasized that one single RIS pixel is not a beamformer but a scatterer [27]. Therefore, a large number of pixels are arranged periodically on the top layer, and the junction capacitance of the varactor diode in each pixel is controlled by the biasing voltage. Consequently, the RIS with a total of M pixels is able to reshape the incident wave[2], and each pixel has *its own unique reflection coefficient.*

B. Approximated Phase-Dependent Amplitudes

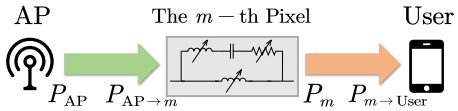

Fig. 2: A downlink cascaded path of the m-th pixel.

Fig. 2 illustrates the m-th downlink cascaded path of the RIS-aided communication. Note that P_{AP}, $P_{\mathrm{AP}\to m}$, P_m, and $P_{m\to\mathrm{User}}$ respectively denote the transmit power by an access point (AP), the received power by the m-th pixel, the reflected power by the m-th pixel, and the received power by a user. Then we have

$$\underbrace{P_{\mathrm{AP}} \overset{(i)}{>} P_{\mathrm{AP}\to m}}_{\text{Fading Channel}} \overbrace{\underset{(ii)}{\geq}}^{\text{RIS}} \underbrace{P_m \overset{(iii)}{>} P_{m\to\mathrm{User}}}_{\text{Fading Channel}}, \tag{4}$$

where (i) and (iii) are caused by large/small-scale fading and non-isotropic pixels [5]. But for (ii), the main reasons are the PSE, the PDA and the PE [10], [18], and (ii) is an equal sign when there is no PE and the PDA is always 1. To characterize reflection amplitudes more accurately, for the m-th pixel, we derive an equivalent low-pass expression for the receiver power without error as

$$P_m = \left|\beta(\phi_m)\exp(-\jmath\phi_m)\right|^2 P_{\mathrm{AP}\to m}, \tag{5}$$

where[3] $\beta(\phi_m)$ is the m-th PDA of the pixel and ϕ_m is the desired phase defined in (3).

Most previous works ignored the PDA $\beta(\phi_m)$ or simply assumed it is a constant smaller than or equal one (e.g., The first two models in Table I). This makes sense if we consider the far-field scenario and each pixel works in the same behavior. However, if the transceiver and the RIS are in the NF case, the pixel has its own feature. In other words, given the different transmission distances between the pixels and the transceiver, we have to not only consider the different phases but also the different distances and other unique characteristics such as the PDA of each scatterer. Considering (2) and defining $\varsigma_m = \beta(\phi_m)\exp(-\jmath\phi_m)$, an ideal equivalent phase shift model was introduced as [18]

[2]A large-area metasurface (i.e., a large number of pixels) is needed to outperform the traditional transmission enhancement techniques such as relaying [26]. Hence $M \gg 1$.

[3]Individual differences in the pixel hardware are ignored in this paper, thus $\beta_1(\cdot) = \beta_2(\cdot) = \cdots = \beta_M(\cdot) = \beta(\cdot)$.

$$\beta(\phi_m) = (1-b)\cdot\left(\frac{\sin(\phi_m - c)+1}{2}\right)^a + b, \tag{6}$$

where $a \geq 1$ is the steepness factor, $b \in [0,1]$ is the minimum amplitude, $c \in (0, \pi/2]$ is the horizontal distance, and all parameters are related to the specific circuit implementation. We call $\beta(\phi_m)$ an *approximated phase-dependent amplitude* (e.g., Case II in Table I). To demonstrate that b is more important than both a and c, we plot Fig. 3a using various parameters. It shows the relationship between phase shift $\phi_m \in [-\pi/2-c, \pi/2+c]$ and reflected amplitude $\beta(\phi_m) \in [b, 1]$. When[4] $\phi_m = \pi/2+c$, the amplitude $\beta(\phi_m)$ is maximized to 1. This is because the reflective currents are out-of-phase with the pixel currents. However, when $\phi_m = -\pi/2 + c$, the amplitude is minimized to b since the dielectric and metallic losses increase [18]. Besides, the approximated PDA model and the circuit model (2) match well, which shows the correctness of (6). From Fig. 3b, it can be observed that the minimum amplitude b is more important than the other parameters[5]. Fig. 3c shows that c does not decrease the amplitude but changes the positions of the peak and the foot. Besides, we present the designed phase shifts feasible set in the complex plane relative to the ideal unit circle under variations in a, b, and c. Based on Fig. 3d increasing a shifts and squeezes the set with a non-monotonic area that shrinks for large a. Fig. 3e shows increasing b roughly scales it up, enlarging the area and approaching the unit circle, and Fig. 3f reveals c mainly causes a global rotation with nearly constant area. Thus, in order to mimic the real pixel device, choosing a suitable b is of great significance. We then have a proposition as follows.

Proposition 2 (Lower and upper bounds of the ideal PDA): *When the pixel hardware and the phase shift are both noiseless, the lower and upper bounds of $\beta(\phi_m)$ in (6) are given by*

$$b \overset{(i)}{\leq} \beta(\phi_m)\big|_{a>1} \overset{(ii)}{\leq} \beta(\phi_m)\big|_{a=1} \overset{(iii)}{\leq} 1. \tag{7}$$

Proof: First, when $\phi_m = \phi_{\mathsf{L}}$, equality holds in (i). Similarly, (ii) holds with equality when $\beta(\phi_m)$ attains its minimum (maximum), respectively. Moreover, since $\sin(\phi_m - c) \in [0,1]$ and $b \in [0,1]$, it is straightforward to verify (iii). This completes the proof. ∎

Based on Fig. 3, b dominates the equivalent phase shift model in (6). Therefore, instead of focusing on $\beta(\phi_m)\big|_{a>1}$, we mainly study $\beta(\phi_m)\big|_{a=1}$ throughout this paper, which can be viewed as a special case of the proposed model $\beta(\phi_m)$. Consequently, we define $\phi_{\mathsf{L}} = -\pi/2 + c$, $\phi_{\mathsf{U}} = \pi/2 + c$, and $\bar{\beta}(\phi_m) = \beta(\phi_m)\big|_{a=1}$ for the remainder of this work. Since a is less significant relative to other parameters, $\bar{\beta}(\phi_m)$ is indicative of the predominant characteristic of $\beta(\phi_m)$.

[4]It's worth mentioning that there is no negative phase in reality, thus for ϕ_m, the actual phase shift should add $2k\pi$ where k is a non-negative integer, and the relationship between ϕ_m and $\beta(\phi_m)$ in (6) is still valid. In this paper, we use $\phi_m \in [-\pi/2-c, \pi/2+c]$ for the convenience of expression. It is easy to find that when $c = \pi/2$, $\phi_m \in [-\pi, \pi]$.

[5]For example, when b is fixed to 0.5, the energy loss between $a = 1.6$ and 2 is just 0.2 dB. However, if a equals 2, the energy loss between $b = 1$ and 0.5 is 3.2 dB. More details can be found in [18].

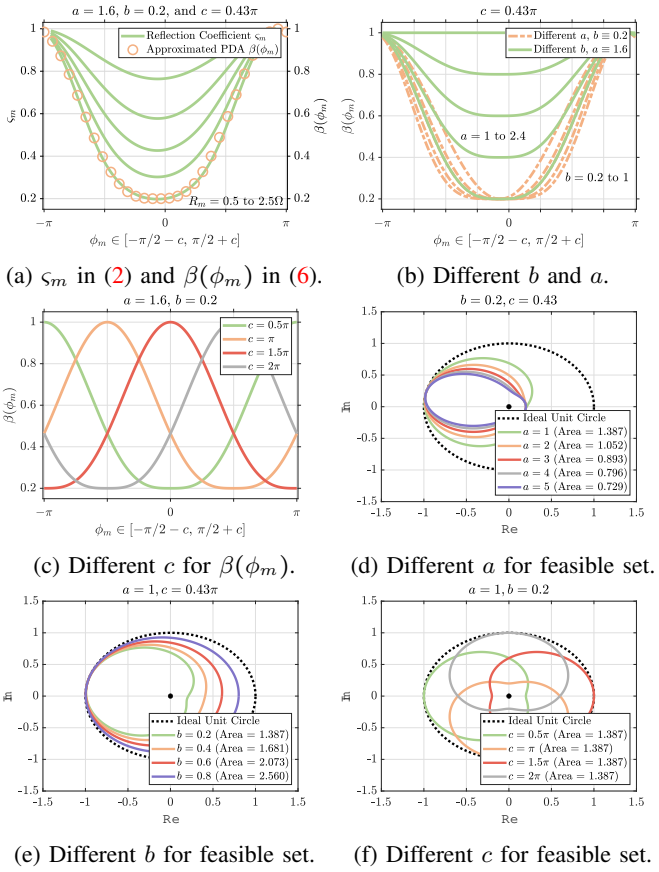

(a) ς_m in (2) and $\beta(\phi_m)$ in (6). (b) Different b and a.

(c) Different c for $\beta(\phi_m)$. (d) Different a for feasible set.

(e) Different b for feasible set. (f) Different c for feasible set.

Fig. 3: Approximated PDA model validations and phase shift feasible set plots. Electrical parameters are from [18].

III. Impacts of Phase Errors on Phase-Dependent Amplitudes

In Sec. II, we introduce the RIS pixel circuit model ς_m in (2) and its approximated equivalent model $\beta(\phi_m)$ in (6). In practice, however, random noise cannot be ignored [10]. The PE is caused by multiple internal and/or external reasons such as hardware degradations, channel estimations, and human-induced accidents [10], [11], [15], [17], [29]. Hence, in this section, we delve into the last four cases outlined in Table I, with a particular focus on the implications of integrating the PE with the PDA. Normally there are three types of PE in the RIS pixel, namely *quantization errors* [11], *hardware aging effects* [17], and *imperfect phase estimations* [10]. The first two PE RVs follow $\mathcal{UF}$ distributions, while the last RV follow $\mathcal{VM}$ distribution. This work considers these three uncertainties.

Suppose there is an RIS with M pixels and each transceiver is equipped with a single isotropic antenna. The total power that is emitted from the RIS[6] can be obtained as $P_{\text{RIS}} = \left|\sum_{m=1}^{M}\sqrt{P_{\text{AP}\to m}}\beta(\phi_m + \bar{\Delta}_m)\exp(-\jmath(\phi_m + \Delta_m))\right|^2$, where Δ_m, $\bar{\Delta}_m$, and $\breve{\Delta}_m$ are RVs. Note that $\bar{\Delta}_m = \iota\Delta_m + \sqrt{1-\iota^2}\breve{\Delta}_m$ and $\breve{\Delta}_m$ is i.i.d. with Δ_m. The coefficient $\iota \in [0,1]$ is introduced to characterizes the correlation between the PE in the PDA (i.e., $\bar{\Delta}_m$) and in the PSE (i.e., Δ_m). When $\iota = 0$,

[6]This is the power that the RIS radiates rather than the receiver receives.

Δ_m and $\bar{\Delta}_m$ are i.i.d., if $\iota = 1$, $\Delta_m = \bar{\Delta}_m$. For intermediate values $\iota \in (0,1)$, Δ_m and $\bar{\Delta}_m$ exhibit partial correlation.

Therefore, assuming that the noise RVs on different pixels (e.g., $m = 1, 2$) are i.i.d., P_{RIS} can be rewritten as

$$\begin{aligned} P_{\mathrm{RIS}} &= \left| \sum_{m=1}^{M} \sqrt{P_{\mathrm{AP}\to m}} \overbrace{\beta(\phi_m + \underbrace{\bar{\Delta}_m}_{\mathrm{PE}})}^{\mathrm{PDA}} \overbrace{\exp(-\jmath \underbrace{\Delta_m}_{\mathrm{PE}})}^{\mathrm{PSE}} \right|^2 \\ &\overset{(i)}{=} P_{\mathrm{AP}\to 1} \left| \sum_{m=1}^{M} \beta(\phi_m + \bar{\Delta}_m) \exp(-\jmath \Delta_m) \right|^2 \\ &= M^2 P_{\mathrm{AP}\to 1} \left| \frac{1}{M} \sum_{m=1}^{M} \beta(\phi_m + \bar{\Delta}_m) \exp(-\jmath \Delta_m) \right|^2 \\ &\xrightarrow{M\to\infty} \underbrace{M^2 P_{\mathrm{AP}\to 1}}_{\text{Square Law}} \underbrace{\left| \mathbb{E}\{\beta(\phi + \bar{\Delta}) \exp(-\jmath \Delta)\} \right|^2}_{\text{Remaining Power } \Gamma \in (0,1)}, \end{aligned} \tag{8}$$

where (i) is obtained when the pixels are all with the same transmit power $P_{\mathrm{AP}\to 1} = P_{\mathrm{AP}\to 2} = \cdots = P_{\mathrm{AP}\to M}$, respectively. As the number of reflecting pixels M becomes sufficiently large, the phase shift set $\{\phi_m\}_{m=1}^{M}$, which is designed to be densely and uniformly distributed over the interval $[-\pi/2 - c, \pi/2 + c]$, form a sequence whose empirical distribution function converges to that of a continuous $\mathcal{UF}$ distribution over $[-\pi/2 - c, \pi/2 + c]$. By considering an extension of the *Glivenko–Cantelli theorem* [7] [30], for the bounded continuous functions $\beta(\phi + \bar{\Delta}) \exp(-\jmath \Delta)$, the final step of (8) is obtained.

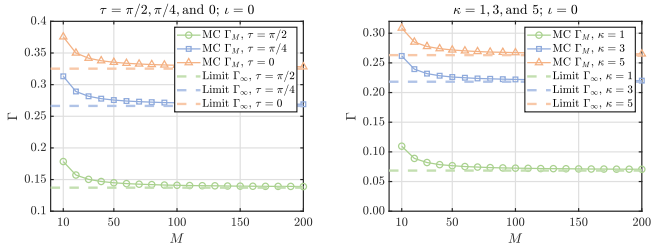

(a) $\mathcal{UF}[\tau, \tau]$ and $\iota = 0$.

(b) $\mathcal{VM}(0, \kappa)$ and $\iota = 0$.

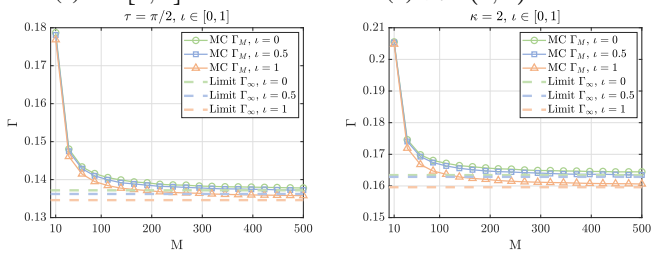

(c) $\mathcal{UF}[\tau, \tau]$ and $\iota \in [0, 1]$.

(d) $\mathcal{VM}(0, \kappa)$ and $\iota \in [0, 1]$.

Fig. 4: Validation of (8).

It can be seen that (8) contains two parts. The first one, i.e., $M^2 P_{\mathrm{AP}\to m}$, reveals that the total power emitted from the RIS P_{RIS} increases directly proportional to M^2. This behavior is also called *square law* in the RIS communication [27]. Moreover, the second part, i.e., normalized *remaining power* Γ, cannot be ignored especially when we consider a practical RIS system. Previous works only considered $|\mathbb{E}\{\exp(-\jmath \Delta_m)\}|^2$. In the rest of this paper, we define $\Gamma = |\mathbb{E}\{\beta(\phi_m + \bar{\Delta}_m) \exp(-\jmath \Delta_m)\}|^2$, which represents the power that remains after a signal passes through an RIS pixel. Besides, it is worth noting that $\phi_1 \neq \phi_2 \neq \cdots \neq \phi_M$ because each pixel experiences its own cascaded fading channel, making an accurate approximation of Γ challenging. Nevertheless, as M grows large, (8) implies that P_{RIS} approaches a constant.

To model the quantization errors and hardware degradations of the RIS, we assume that the PEs δ_m and $\bar{\delta}_m$ at the m-th pixel follow a $\mathcal{UF}$ distribution [10], i.e., δ_m and $\bar{\delta}_m \sim \mathcal{UF}[-\tau, \tau]$, where $\tau \in [0, \pi/2]$. The corresponding probability density function (PDF) is $f_{\mathcal{UF}}(\delta) = \frac{1}{2\tau}$ where $\delta \in [-\tau, \tau]$ or is zero otherwise. Hence, the reflection coefficient is $\beta(\phi_m + \bar{\delta}_m) \exp(-\jmath(\phi_m + \delta_m))$, where $\bar{\delta}_m = \iota \delta_m + \sqrt{1 - \iota^2} \breve{\delta}_m$, $\iota \in [0, 1]$ and $\breve{\delta}_m$ is i.i.d. with δ_m. For imperfect channel estimations of the RIS, we assume that the errors γ_m and $\bar{\gamma}_m$ in the m-th pixel follows zero-mean $\mathcal{VM}$ distributions [31], i.e., γ_m and $\bar{\gamma}_m \sim \mathcal{VM}(0, \kappa)$, where κ is concentration parameter. Accordingly, the PDF is $f_{\mathcal{VM}}(\gamma) = \frac{\exp(\kappa \cos(\gamma))}{2\pi I_0(\kappa)}$ where $\gamma \in [-\pi, \pi]$ and $I_n(\kappa)$ is the modified Bessel function of the first kind of order n with $\kappa \geq 1$. Thus, the reflection coefficient is $\beta(\phi_m + \bar{\gamma}_m) \exp(-\jmath(\phi_m + \gamma_m))$, where $\bar{\gamma}_m = \iota \gamma_m + \sqrt{1 - \iota^2} \breve{\gamma}_m$, $\iota \in [0, 1]$ and $\breve{\gamma}_m$ is i.i.d. with γ_m.

It can be observed from Figs. 4a and 4b that, when $\iota = 0$, as M increases from 1 to 200, Monte Carlo (MC) result $\Gamma_M = \left| \frac{1}{M} \sum_{m=1}^{M} \beta(\phi_m + \bar{\Delta}_m) \exp(-\jmath \Delta_m) \right|^2$ converges asymptotically to analytical (AN) limit $\Gamma_\infty = \left| \mathbb{E}\{\beta(\phi + \bar{\Delta}) \exp(-\jmath \Delta)\} \right|^2$. Besides, as the PE becomes more severe (i.e., τ increases from 0 to $\pi/2$ and κ increases from 1 to 5), Γ_M and Γ_∞ decrease accordingly. Besides, from Figs. 4c and 4d, if $\iota = 1$, the same convergence behavior is observed, i.e., as M grows from 1 to 500, the MC result Γ_M approaches its AN limit Γ_∞. More importantly, both Γ_M and Γ_∞ with $\iota = 1$ are smaller than these with $\iota = 0$. This implies if an RIS has a sufficiently large number of pixels (e.g., $M > 200$ when $\iota = 0$ and $M > 500$ when $\iota = 1$) and the average phase approaches zero, then fully coupled noise (i.e., $\iota = 1$) is more detrimental than i.i.d. noise (i.e., $\iota = 0$). The top row of Fig. 5 plots the characteristics of $\bar{\delta}_m = \iota \delta_m + \sqrt{1 - \iota^2} \breve{\delta}_m$ when i.i.d. RVs δ and $\breve{\delta}_m$ follow a $\mathcal{UF}$ distribution with $\tau = \pi/2$. As the correlation coefficient ι increases from 0 to 1, the scatter points transition from occupying a square region to converging along the diagonal, fully aligning at $\iota = 1$. In the third figure of this row, the overall trend of the green dots is flatter than the orange line. This is because the best-fit line for the green dots is not the line $\bar{\delta}_m = \delta_m$, but rather $\bar{\delta}_m = 0.75 \delta_m$. The bottom row of Fig. 5 presents the same construction method and i.i.d. RVs γ and $\breve{\gamma}_m$ follow a $\mathcal{VM}$ distribution. As ι increases, the correlation strengthens and points cluster toward the diagonal, yet the central concentration of the $\mathcal{VM}$ and sparse tails result in higher density at the center. In the rest of this section, we study the last four cases in Table I as follows[8].

[7] If the empirical distribution of a deterministic sequence converges weakly, the function average over the sequence approaches the corresponding expectation

[8] In Cases II, III, and IV, we assume $\phi_1 = \phi_2 = \cdots = \phi_m$ so that the effect of uncertainties can be examined under a fixed phase shift.

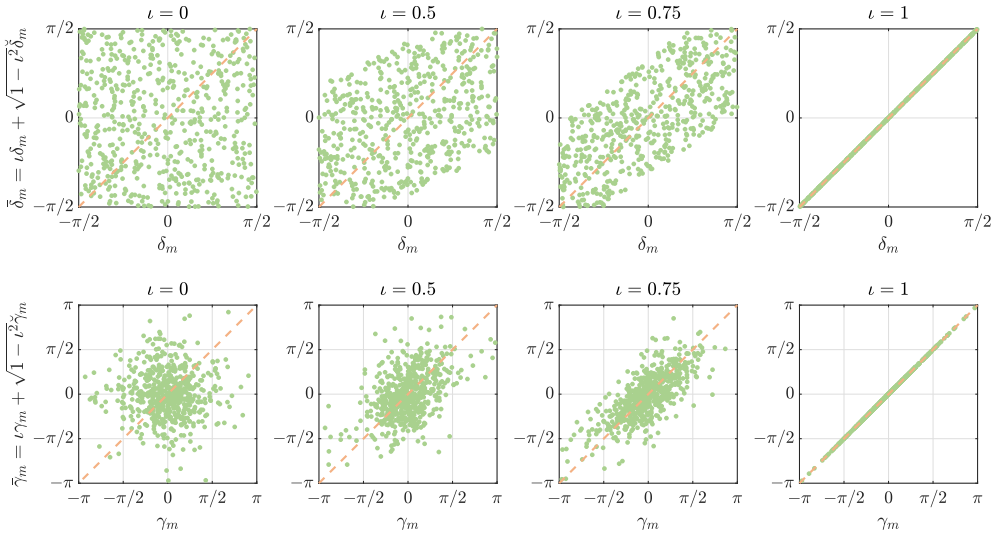

Fig. 5: Scatter plots of $\mathcal{UF}$ and $\mathcal{VM}$ RVs for different correlation coefficients $\iota \in [0, 0.5, 0.75, 1]$.

A. Case I: When the PDA is A Constant

When the PDA of the m-th pixel is a constant for all M pixels and only the PSE contains the PE, we have the RP Γ as

$$\Gamma = \underbrace{\left|\mathbb{E}\left\{\beta \exp(-\jmath\Delta_m)\right\}\right|^2}_{\text{Case I}}, \tag{9}$$

where $\Delta_m = \delta_m$ or γ_m. Consequently, the impact of noise on Γ can be described by the following two propositions.

Proposition 3.1 $\left(\beta\exp(-\jmath\delta_m)\right.$, the PDA is a constant and only the PSE contains $\mathcal{UF}$ RVs$\left.\right)$: *When the m-th PDA is a constant β, and the PSE includes $\delta_m \sim \mathcal{UF}[-\tau, \tau]$ where $\tau \in [0, \pi/2]$, then the RP Γ in (10) can be obtained as*[9]

$$\begin{aligned}\Gamma_{(3.1)} &= \left|\mathbb{E}\left\{\beta \exp(-\jmath\delta_m)\right\}\right|^2 \\ &= \beta^2\left(1 - \frac{1}{3}\tau^2 + \frac{2}{45}\tau^4 - \frac{1}{360}\tau^6 + \frac{1}{14400}\tau^8\right) + \mathcal{O}\left(\tau^{10}\right),\end{aligned} \tag{10}$$

where $\mathcal{O}(\cdot)$ denotes higher-order terms.

Proof: Please see Appendix A in [1]. ■

Fig. 6a reveals that $\Gamma_{(3.1)}$ needs at least the first three terms of the Taylor series expansion of $\sin(\tau)$. The error term[10] is $\Gamma^{\text{Error}}_{(3.1)} = \left|\Gamma^{\text{MC}}_{(3.1)} - \Gamma^{\text{AN}}_{(3.1)}\right| \sim \mathcal{O}(\tau^{10})$ and becomes significant when τ approaches $\pi/2$.

Proposition 3.2 $\left(\beta\exp(-\jmath\gamma_m)\right.$, the PDA is a constant and only the PSE contains $\mathcal{VM}$ noises$\left.\right)$: *When the m-th PDA is a constant β, and the PSE includes $\gamma_m \sim \mathcal{VM}(0, \kappa)$ where $\kappa \geq 1$, then the RP Γ in (9) can be obtained as*

$$\Gamma_{(3.2)} = \left|\mathbb{E}\left\{\beta \exp(-\jmath\gamma_m)\right\}\right|^2 = \beta^2\rho^2, \tag{11}$$

[9]Except for special instructions, we assume in the remaining part of this paper that $\Gamma_{(\cdot)} = \Gamma_{(\cdot)}(\phi_m)$.

[10]For clarity, we smooth the error curves without affecting their accuracy.

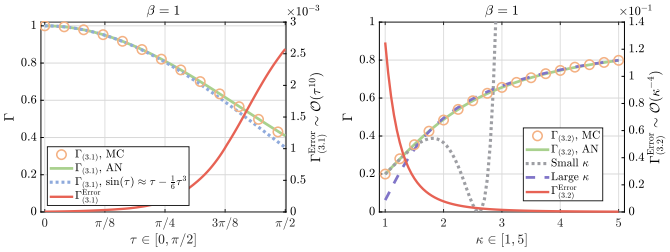

(a) Validation of Proposition 3.1. (b) Validation of Proposition 3.2.

Fig. 6: Validation of Case I.

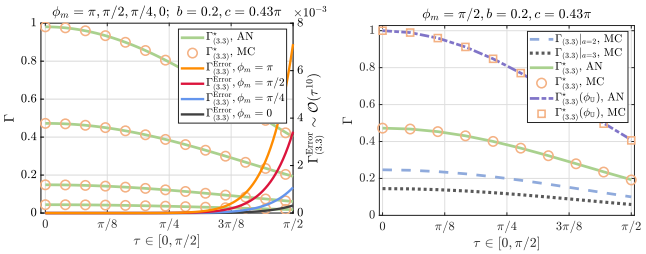

(a) Validation of $\Gamma^{\star}_{(3.3)}$. (b) Validation of Prop. 3.3.

Fig. 7: Validation of Prop. 3.3.

where

$$\rho = \begin{cases} \frac{\kappa}{2}\left(1 - \frac{\kappa^2}{8} + \frac{\kappa^4}{48} - \frac{11\kappa^6}{3072}\right) + \mathcal{O}(\kappa^9) & \text{for small } \kappa \\ 1 - \frac{1}{2\kappa} - \frac{1}{8\kappa^2} - \frac{1}{8\kappa^3} + \mathcal{O}(\kappa^{-4}) & \text{for large } \kappa. \end{cases} \tag{12}$$

Proof: Please see Appendix A. ■

From Fig. 6b, we can see that if $\kappa \in [1, 1.6]$, $\frac{\kappa}{2}\left(1 - \frac{\kappa^2}{8} + \frac{\kappa^4}{48} - \frac{11\kappa^6}{3072}\right)$ is a suitable approximation of ρ, otherwise we should use $1 - \frac{1}{2\kappa} - \frac{1}{8\kappa^2} - \frac{1}{8\kappa^3}$. For small κ, ρ^2 incurs a truncation error of $\Gamma^{\text{Error}}_{(3.2)} \sim \mathcal{O}(\kappa^9)$. In contrast, for large κ, the asymptotic expansion yields an error of $\Gamma^{\text{Error}}_{(3.2)} \sim \mathcal{O}(\kappa^{-4})$. To

ensure correctness and reproducibility, $\mathcal{VM}$ RVs are generated using CircStat [32] and vmrand [33] in this paper.

B. Case II: When the PDA is without Phase Errors

When the PDA of the m-th pixel is $\beta(\phi_m)$ in (6) without any errors and the PSE is with the PE, we have the RP Γ as

$$\Gamma = \underbrace{\boxed{\left|\mathbb{E}\left\{\beta(\phi_m)\exp(-\jmath\Delta_m)\right\}\right|^2}}_{\text{Case II}}, \tag{13}$$

where $\Delta = \delta_m$ or γ_m. Hence, the impact of noise on Γ can be described by the following two propositions.

Proposition 3.3 *($\beta(\phi_m)\exp(-\jmath\delta_m)$, the PDA is ideal and the PSE contains $\mathcal{UF}$ RVs): When the m-th PDA is $\beta(\phi_m)$ and without any noises, and the PSE includes $\delta_m \sim \mathcal{UF}[-\tau,\tau]$ where $x \in [0,\pi/2]$, then the upper bounds of the RP Γ in (13) can be obtained as*

$$\Gamma_{(3.3)} \overset{(i)}{\leq} \Gamma^{\star}_{(3.3)} < \Gamma^{\star}_{(3.3)}(\phi_{\mathsf{U}}), \tag{14}$$

where $\Gamma_{(3.3)} = \left|\mathbb{E}\left\{\beta(\phi_m)\exp(-\jmath\delta_m)\right\}\right|^2$, $\Gamma^{\star}_{(3.3)} = \left|\mathbb{E}\left\{\bar{\beta}(\phi_m)\exp(-\jmath\delta_m)\right\}\right|^2 = \zeta\big(1 - \frac{1}{3}\tau^2 + \frac{2}{45}\tau^4 - \frac{1}{360}\tau^6 + \frac{1}{14400}\tau^8\big) + \mathcal{O}\big(\tau^{10}\big)$ *and* $\zeta = \frac{(1-b)^2}{4}\sin^2(\phi_m - c) + \frac{(1-b^2)}{2}\sin(\phi_m - c) + \frac{(1+b)^2}{4}$. $\Gamma^{\star}_{(3.3)}(\phi_{\mathsf{U}}) = \big(1 - \frac{1}{3}\tau^2 + \frac{2}{45}\tau^4 - \frac{1}{360}\tau^6 + \frac{1}{14400}\tau^8\big)$. *Moreover, the equality in (i) is satisfied when*[11] *$a = 1$.* $\Gamma^{\star}_{(3.3)} \sim \mathcal{O}(\tau^{10})$.

Proof: Please see Appendix B in [1]. ∎

It is not difficult to find that $b^2 \leq \zeta \leq 1$, and b^2 and 1 can be obtained respectively when $\phi_m = \phi_{\mathsf{L}}$ and ϕ_{U}. Besides, Fig. 7a reveals an important insight that different ϕ_m are affected differently by the same error. In particular, if $\phi_m = \pi$, the RP decreases from 1 to 0.4 when τ increase from 0 to $\pi/2$. However, when $\phi_m = \pi/4$, the RP decrease can be ignored even τ approaches to $\pi/2$. The error term is $\Gamma^{\text{Error}}_{(3.3)} = \left|\Gamma^{\text{MC}}_{(3.3)} - \Gamma^{\text{AN}}_{(3.3)}\right| \sim \mathcal{O}(\tau^{10})$. Fig. 7b illustrates that when $\phi_m = \phi_{\mathsf{U}}$, the RIS pixel always has full reflections, i.e., $\beta(\phi_m)$ is maximized to 1. However, in practice, ϕ_{U} cannot align M paths to the receiver. Therefore, $\Gamma^{\star}_{(3.3)}(\phi_{\mathsf{U}})$ represents the upper bound on RP resulting from maximizing amplitude, rather than aiming to enhance the overall performance of the system. A well-designed ϕ_m in $\Gamma^{\star}_{(3.3)}$ denotes a trade-off between maximizing the PDA and aligning cascaded channels.

Proposition 3.4 *($\beta(\phi_m)\exp(-\jmath\gamma_m)$, the PDA is ideal and the PSE contains $\mathcal{VM}$ RVs): When the m-th PDA is $\beta(\phi_m)$ and without any errors, and the PSE includes $\gamma_m \sim \mathcal{VM}(0,\kappa)$ where $\kappa \geq 1$, then the upper bounds of the RP Γ in (13) can be obtained as*

$$\Gamma_{(3.4)} \leq \Gamma^{\star}_{(3.4)} < \Gamma^{\star}_{(3.4)}(\phi_{\mathsf{U}}), \tag{15}$$

where $\Gamma_{(3.4)} = \left|\mathbb{E}\left\{\beta(\phi_m)\exp(-\jmath\gamma_m)\right\}\right|^2$, $\Gamma^{\star}_{(3.4)} = \left|\mathbb{E}\left\{\bar{\beta}(\phi_m)\exp(-\jmath\gamma_m)\right\}\right|^2 = \zeta\rho^2$, $\Gamma^{\star}_{(3.4)}(\phi_{\mathsf{U}}) = \rho^2$, *and ρ and ζ are the same as they in Props. 3.2 and 3.3, respectively.*

[11] This condition also applies to Propositions 3.4 to 3.10.

Proof: The proof is the same as Props. 3.1 to 3.3 and is omitted here. ∎

When the concentration parameter κ increases, the distribution of directions becomes more concentrated around the mean direction 0, and the RP grows. The error term is $\Gamma^{\text{Error}}_{(3.4)} = \left|\Gamma^{\text{MC}}_{(3.4)} - \Gamma^{\text{AN}}_{(3.4)}\right| \sim \mathcal{O}(\kappa^{10})$. When $\kappa = 0$, the $\mathcal{VM}$ distribution reduces to a $\mathcal{UF}$ distribution. It can be observed from Fig. 8a that when $\kappa = 1$, the RP is from 0 to 0.2 when $\phi_m = 0$ to π. When $\kappa = 5$ and $\phi_m = \pi$, the RP achieves to 0.8. However, even $\kappa = 5$, $\Gamma^{\star}_{(3.4)}$ is still limited as $\phi_m = 0$. Therefore, the PE is no longer important when ϕ_m approaches 0, because the amplitude available for unitize at this time is already at its lowest value. Besides, Fig. 8b shows the correctness of (15).

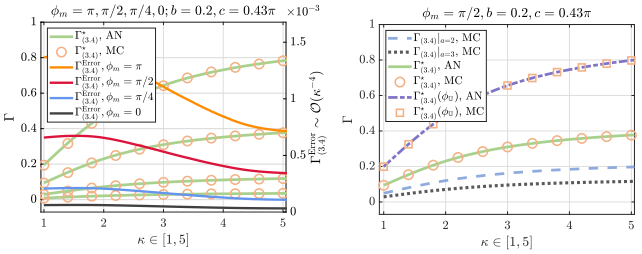

(a) Validation of $\Gamma^{\star}_{(3.4)}$. (b) Validation of Prop. 3.4.

Fig. 8: Validation of Prop. 3.4.

C. Case III: When the PDA is with Single Error

When the PDA of the m-th pixel is the approximated model (6) with $\bar{\Delta}_m$ and the PSE is with Δ_m, we have the RP Γ as

$$\Gamma = \underbrace{\boxed{\left|\mathbb{E}\left\{\beta(\phi_m + \bar{\Delta}_m)\exp(-\jmath\Delta_m)\right\}\right|^2}}_{\text{Case III}}, \tag{16}$$

where $\Delta_m = \delta_m$ or γ_m, $\bar{\Delta}_m = \delta_m$ or γ_m, and Δ_m and $\bar{\Delta}_m$ are the same or i.i.d. Hence, the impact of noise on Γ can be described by the following four propositions.

Proposition 3.5 *($\beta(\phi_m + \delta_m)\exp(-\jmath\delta_m)$, $\iota = 1$): When $\iota = 1$, the m-th PDA is $\beta(\phi_m + \delta_m)$, and the PDA and the PSE all contain $\delta_m \sim \mathcal{UF}[-\tau,\tau]$ where $\tau \in [0,\pi/2]$, then the upper bound of the RP Γ in (16) can be obtained as*

$$\Gamma_{(3.5)} \leq \Gamma^{\star}_{(3.5)} = (\eta_1 + \eta_2)^2 + \eta_3 < \Gamma^{\star}_{(3.5)}(\phi_{\mathsf{U}}), \tag{17}$$

where $\Gamma_{(3.5)} = \left|\mathbb{E}\{\beta(\phi_m + \delta_m)\exp(-\jmath\delta_m)\}\right|^2$, $\Gamma^{\star}_{(3.5)} = \left|\mathbb{E}\{\bar{\beta}(\phi_m + \delta_m)\exp(-\jmath\delta_m)\}\right|^2$, $\eta_1 = \frac{(1-b)}{2}\sin(\phi_m - c)\big(1 - \frac{1}{3}\tau^2 + \frac{1}{15}\tau^4 - \frac{2}{315}\tau^6\big) + \mathcal{O}(\tau^8)$, $\eta_2 = \frac{1+b}{2}\big(1 - \frac{1}{6}\tau^2 + \frac{1}{120}\tau^4 - \frac{1}{5040}\tau^6\big) + \mathcal{O}(\tau^8)$, $\eta_3 = \frac{(1-b)^2}{4}\big(\frac{1}{3}\tau^2 - \frac{1}{15}\tau^4 + \frac{2}{315}\tau^6\big)^2\cos^2(\phi_m - c) + \mathcal{O}(\tau^{12})$, $\Gamma^{\text{Error}}_{(3.5)} = \left|\Gamma^{\text{MC}}_{(3.5)} - \Gamma^{\text{AN}}_{(3.5)}\right| \sim \mathcal{O}(\tau^8)$. $\Gamma^{\star}_{(3.5)}(\phi_{\mathsf{U}}) = \big(\eta_1/\sin(\phi_m - c) + \eta_2\big)^2$.

Proof: Please see Appendix C in [1]. ∎

From Fig. 9a, it can be seen that the approximated AN expression of $\Gamma^{\star}_{(3.5)}$ is correct. Besides, when the amplitude is large (e.g., $\phi_m = \pi$), the impact of the PE δ_m on the PDA is more significant. Besides, the AN and the MC results

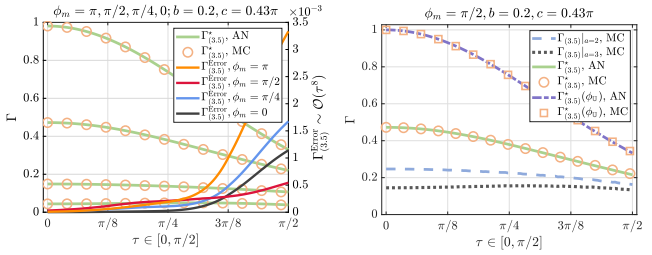

(a) Validation of $\Gamma^{\star}_{(3.5)}$. (b) Validation of Prop. 3.5.

Fig. 9: Validation of Prop. 3.5.

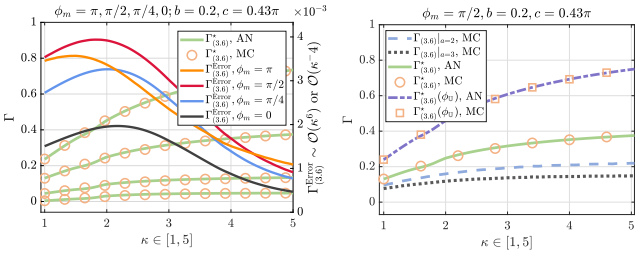

(a) Validation of $\Gamma^{\star}_{(3.6)}$. (b) Validation of Prop. 3.6.

Fig. 10: Validation of Prop. 3.6.

exhibits a noticeable deviation when $\phi_m = \pi$ and $\tau = \pi/2$ since the approximation expression of $\Gamma^{\star}_{(3.5)}$ utilizes a Taylor expansion at $x = 0$. If the amplitude of PDA is large, then the approximation will be somewhat inaccurate when $\tau = \pi/2$. Fig. 9b shows that Γ of $a = 2$ and 3 are all small and they are not influenced by the PE δ_m very seriously. Moreover, $\Gamma^{\star}_{(3.5)}(\phi_{\mathsf{U}})$ performs best since $\phi_{\mathsf{U}} = \pi/2 + c$ offers the highest $\beta(\phi_m)$, but this strategy may lead to the mismatch on the phases of the cascaded and/or direct links.

Remark I (In Fig. 9a, why $\phi_m = \pi/2$ has the smallest error when ϕ_m is close to $\pi/2$?): *In Fig.9a, the error is smallest when ϕ_m is close to $\pi/2$, because the PDA is less sensitive to the PE near this point. Specifically, in the PDA model, at $\phi_m \approx \pi/2$, the derivative $\partial\beta(\phi_m)/\partial\phi_m$ is small, resulting in milder changes in it when adding δ_m. Thus, the Taylor expansion approximation based on small τ is more accurate, with reduced impact from higher-order terms, leading to the minimal error.*

Proposition 3.6 $\left(\beta(\phi_m + \gamma_m)\exp(-\jmath\gamma_m),\ \iota = 1\right)$: *When $\iota = 1$, the m-th PDA is $\beta(\phi_m + \gamma_m)$, and the PDA and the PSE all contain $\gamma_m \sim \mathcal{VM}(0,\kappa)$ where $\kappa \geq 1$, then the upper bounds of the RP Γ in (16) can be obtained as*

$$\Gamma_{(3.6)} \leq \Gamma^{\star}_{(3.6)} = (\eta_1 + \eta_2)^2 + \eta_3 < \Gamma^{\star}_{(3.6)}(\phi_{\mathsf{U}}), \tag{18}$$

where $\Gamma_{(3.6)} = \left|\mathbb{E}\{\beta(\phi_m + \gamma_m)\exp(-\jmath\gamma_m)\}\right|^2$, $\Gamma^{\star}_{(3.6)} = \left|\mathbb{E}\{\bar{\beta}(\phi_m + \gamma_m)\exp(-\jmath\gamma_m)\}\right|^2$, $\eta_1 = \frac{1+b}{2}\rho$, $\eta_2 = \frac{1-b}{4}\sin(\phi_m - c)(1+\bar{\rho})$, *and* $\eta_3 = \frac{(1-b)^2}{16}\cos^2(\phi - c)(1-\bar{\rho})^2$. $\Gamma^{\star}_{(3.6)}(\phi_{\mathsf{U}}) = \left(\eta_1 + \frac{(1-b)(1+\bar{\rho})}{4}\right)^2$. *Note $\bar{\rho}$ is defined as*

$$\bar{\rho} = \begin{cases} \frac{\kappa^2}{8}\left(1 - \frac{\kappa^2}{6} + \frac{11\kappa^4}{384}\right) + \mathcal{O}(\kappa^6) & \text{for small } \kappa \\ 1 - \frac{2}{\kappa} + \frac{1}{\kappa^2} - \frac{1}{4\kappa^3} + \mathcal{O}(\kappa^{-4}) & \text{for large } \kappa. \end{cases} \tag{19}$$

Proof: The proof is similar to that of Prop. 3.2 and is omitted here.

Note that $\Gamma^{\text{Error}}_{(3.6)} = \left|\Gamma^{\text{MC}}_{(3.6)} - \Gamma^{\text{AN}}_{(3.6)}\right| \sim \mathcal{O}(\kappa^6)$ or κ^{-4}. Fig. 10a shows the correctness of the approximation of $\Gamma^{\star}_{(3.6)}$. The error first increases and then decreases due to (19). Fig. 10b shows the correctness of (18).

Proposition 3.7 $\left(\beta(\phi_m + \bar{\delta}_m)\exp(-\jmath\delta_m),\ \iota = 0\right)$: *When $\iota = 0$, the m-th PDA is $\beta_m(\phi_m + \bar{\delta}_m)$, and the PDA and the PSE respectively contain $\bar{\delta}_m \sim \mathcal{UF}[-\tau,\tau]$ and $\delta_m \sim \mathcal{UF}[-\tau,\tau]$, where $\tau \in [0, \pi/2]$ and $\bar{\delta}$ and δ are i.i.d, then the upper bounds of the RP Γ in (16) can be obtained as*

$$\Gamma_{(3.7)} \leq \Gamma^{\star}_{(3.7)} = \eta_1^2\eta_2^2 < \Gamma^{\star}_{(3.7)}(\phi_{\mathsf{U}}), \tag{20}$$

where $\Gamma_{(3.7)} = \left|\mathbb{E}\{\beta(\phi_m + \bar{\delta}_m)\exp(-\jmath\delta_m)\}\right|^2$, $\Gamma^{\star}_{(3.7)} = \left|\mathbb{E}\{\bar{\beta}(\phi_m + \bar{\delta}_m)\exp(-\jmath\delta_m)\}\right|^2$, $\eta_1 = \frac{(1-b)}{2}\sin(\phi_m - c)\eta_2 + \frac{(1+b)}{2}$, *and* $\eta_2 = 1 - \frac{1}{6}\tau^2 + \frac{1}{120}\tau^4 + \mathcal{O}(\tau^6)$. $\Gamma^{\star}_{(3.7)}(\phi_{\mathsf{U}}) = \left(\frac{1-b}{2}\eta_2 + \frac{1+b}{2}\right)^2\eta_2^2$.

Proof: The proof is the same as Propositions 3.1, 3.3 and 3.5 and it is omitted here. ■

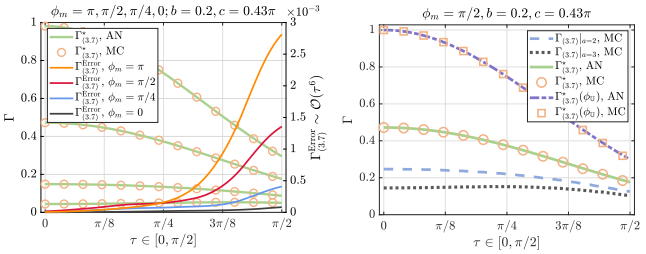

(a) Validation of $\Gamma^{\star}_{(3.7)}$. (b) Validation of Prop. 3.7.

Fig. 11: Validation of Prop. 3.7.

Note that $\Gamma^{\text{Error}}_{(3.7)} = \left|\Gamma^{\text{MC}}_{(3.7)} - \Gamma^{\text{AN}}_{(3.7)}\right| \sim \mathcal{O}(\tau^6)$. Fig. 11a shows the correctness of the approximation of $\Gamma^{\star}_{(3.7)}$. Fig. 11b shows the correctness of (20).

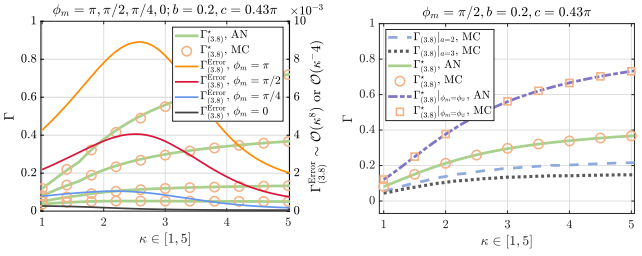

(a) Validation of $\Gamma^{\star}_{(3.8)}$. (b) Validation of Prop. 3.8.

Fig. 12: Validation of Prop. 3.8.

Proposition 3.8 $\left(\beta(\phi_m + \bar{\gamma}_m)\exp(-\jmath\gamma_m),\ \iota = 0\right)$: *When the m-th PDA is $\beta_m(\phi_m + \bar{\gamma}_m)$, the PDA and the PSE respectively contain $\bar{\gamma}_m \sim \mathcal{VM}(0,\kappa)$ and $\gamma_m \sim \mathcal{VM}(0,\kappa)$ where $\kappa \geq 1$, and $\bar{\gamma}_m$ and γ_m are i.i.d., then the upper bounds of the RP Γ in (16) can be obtained as*

$$\Gamma_{(3.8)} \leq \Gamma^{\star}_{(3.8)} = \eta^2\rho^2 < \Gamma^{\star}_{(3.8)}(\phi_{\mathsf{U}}), \tag{21}$$

where $\Gamma_{(3.8)} = \left|\mathbb{E}\left\{\beta(\phi_m + \bar{\gamma}_m)\exp(-\jmath\gamma_m)\right\}\right|^2$, $\Gamma^{\star}_{(3.8)} = \left|\mathbb{E}\left\{\bar{\beta}(\phi_m + \bar{\gamma}_m)\exp(-\jmath\gamma_m)\right\}\right|^2$, $\eta = \frac{(1-b)}{2}\sin(\phi_m - c)\rho + \frac{(1+b)}{2}$, *and* $\Gamma^{\star}_{(3.8)}(\phi_{\mathsf{U}}) = \left(\frac{1-b}{2}\rho + \frac{1+b}{2}\right)^2\rho^2$.

Proof: Consider Appendices A, the proof is obvious.

Note that $\Gamma^{\text{Error}}_{(3.8)} = \left|\Gamma^{\text{MC}}_{(3.8)} - \Gamma^{\text{AN}}_{(3.8)}\right| \sim \mathcal{O}(\kappa^6)$ or $\mathcal{O}(\kappa^{-4})$. Fig. 12a shows the correctness of the approximation of $\Gamma^{\star}_{(3.8)}$. The error first increases and then decreases due to (12). Fig. 12b shows the correctness of (21).

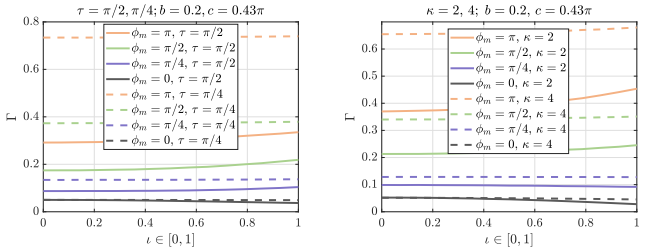

(a) Γ with $\mathcal{UF}$ RVs. (b) Γ with $\mathcal{VM}$ RVs.

Fig. 13: ι vs. Γ considering $\mathcal{UF}$ and $\mathcal{VM}$ RVs.

Remark II (If ϕ_m approaches to 0, why Γ decreases when ι increases?): *As observed in Figs. 13a and 13b, the RP* Γ *decreases as* ϕ_m *approaches* 0. *For instance,* Γ *is slightly lower at* $\phi_m \approx 0$ *than at* $\phi_m \approx \pi/4$. *This is because when* $\phi_m \approx 0$, *the system operates near the linear region of the phase response function* $\beta(\cdot)$. *As the correlation coefficient* ι *increases from* 0 *toward* 1, *the amplitude and phase noise become increasingly coupled. This coupling induces a negative covariance between the amplitude and the phase. We provide a strict proof of* $\Gamma(0)|_{\iota=0} > \Gamma(0)|_{\iota=1}$ *in Appendix B. Fig. 14 verify this remark through MC simulations of vector field distributions under* $\mathcal{UF}$ *and* $\mathcal{VM}$ *RVs, respectively. In particular, when* $\phi_m = 0$, *length of the synthesized vector* $|\mathsf{P}_{\iota=1}| < |\mathsf{P}_{\iota=0}|$ *and the inequality is reversed when* $\phi_m = \pi/2$.

D. Case IV: When the PDA is with Both Errors

When the PDA contains both $\bar{\Delta}_m$ and $\bar{\Theta}_m$ and the PSE also contains both Δ_m and Θ_m, we have the RP Γ as

$$\Gamma = \underbrace{\boxed{\left|\mathbb{E}\left\{\beta(\phi_m + \bar{\Delta}_m + \bar{\Theta}_m)\exp(-\jmath(\Delta_m + \Theta_m)\right\}\right|^2}}_{\text{Case IV}}, \quad (22)$$

where $\bar{\Delta}_m$ and Δ_m are $\mathcal{UF}$ RVs, $\bar{\Delta}_m = \Delta_m$ or they are i.i.d. $\bar{\Theta}_m$ and Θ_m are $\mathcal{VM}$ RVs, $\bar{\Theta}_m = \Theta_m$ or they are i.i.d. Therefore, the impact of noise on Γ can be described by the following two propositions.

Proposition 3.9 $\left(\beta(\phi_m + \delta_m + \gamma_m)\exp(-\jmath(\delta_m + \gamma_m)\right)$, the PDA and the PSE are all with δ_m and γ_m, $\iota = 1$): *When* $\iota = 1$, *the* m*-th PDA is* $\beta(\phi_m + \delta_m + \gamma_m)$, *and the PDA and the PSE all contain* $\delta_m \sim \mathcal{UF}[-\tau, \tau]$ *where* $\tau \in [0, \pi/2]$ *and* $\gamma_m \sim \mathcal{VM}(0, \kappa)$ *where* $\kappa \geq 1.6$, *then the upper bounds of the RP* Γ *in* (8) *can be obtained as*

$$\Gamma_{(3.9)} \leq \Gamma^{\star}_{(3.9)} \quad (23)$$

$$= \left(\frac{(1-b)\sin(\phi_m - c)}{2}(\eta_1 - \eta_4) + \frac{1+b}{2}\eta_5\right)^2 + \frac{(1-b)^2\cos^2(\phi_m - c)}{4}(\eta_2 + \eta_3)^2 < \Gamma^{\star}_{(3.9)}(\phi_{\mathsf{U}}), \quad (24)$$

where $\Gamma_{(3.9)} = \left|\mathbb{E}\left\{\beta(\phi_m + \delta_m + \gamma_m)\exp(-\jmath(\delta_m + \gamma_m))\right\}\right|^2$, $\Gamma^{\star}_{(3.9)} = \left|\mathbb{E}\left\{\bar{\beta}(\phi_m + \delta_m + \gamma_m)\exp(-\jmath(\delta_m + \gamma_m))\right\}\right|^2$, $\eta_1 = \left(1 - \frac{\tau^2}{3} + \frac{\tau^4}{15} - \frac{2\tau^6}{315} + \mathcal{O}(\tau^8)\right)\left(1 - \frac{1}{8\kappa} - \frac{1}{64\kappa^2} - \frac{1}{128\kappa^3} + \mathcal{O}(\kappa^{-4})\right)$, $\eta_2 = \left(\frac{\tau^2}{3} - \frac{\tau^4}{15} + \frac{2\tau^6}{315} + \mathcal{O}(\tau^8)\right)\left(1 - \frac{1}{8\kappa} - \frac{1}{64\kappa^2} - \frac{1}{128\kappa^3} + \mathcal{O}(\kappa^{-4})\right)$, $\eta_3 = \left(1 - \frac{\tau^2}{3} + \frac{\tau^4}{15} - \frac{2\tau^6}{315} + \mathcal{O}(\tau^8)\right)\left(\frac{1}{8\kappa} + \frac{1}{64\kappa^2} + \frac{1}{128\kappa^3} + \mathcal{O}(\kappa^{-4})\right)$, $\eta_4 = \left(\frac{\tau^2}{3} - \frac{\tau^4}{15} + \frac{2\tau^6}{315} + \mathcal{O}(\tau^8)\right)\left(\frac{1}{8\kappa} + \frac{1}{64\kappa^2} + \frac{1}{128\kappa^3} + \mathcal{O}(\kappa^{-4})\right)$, and $\eta_5 = \left(1 - \frac{\tau^2}{6} + \frac{\tau^4}{120} + \mathcal{O}(\tau^6)\right)\left(1 - \frac{1}{2\kappa} - \frac{1}{8\kappa^2} - \frac{1}{8\kappa^3} + \mathcal{O}(\kappa^{-4})\right)$.

Proof: Please see Appendix C. ∎

Fig. 15a verifies the accuracy of the approximation for $\Gamma^{\star}_{(3.9)}$. Fig. 15b validates the exact expression of Prop. 3.9 by directly performing numerical integration of $\Gamma^{\star}_{(3.9)}$. Given that $\Gamma^{\text{Error}}_{(3.9)}$ is on the order of 10^{-2}, consider use direct numerical integration rather than an approximation

Proposition 3.10 $\left(\beta(\phi_m + \bar{\delta}_m + \bar{\gamma}_m)\exp(-\jmath(\delta_m + \gamma_m)\right)$, the PDA are with $\bar{\delta}_m$ and $\bar{\gamma}_m$, and the PSE are with δ_m and γ_m, $\iota = 0$): *When* $\iota = 0$, *the* m*-th PDA is* $\beta_m(\phi_m + \bar{\delta}_m + \bar{\gamma}_m)$, *and it contains* $\bar{\delta}_m \sim \mathcal{UF}[-\tau, \tau]$ *and* $\bar{\gamma}_m \sim \mathcal{VM}(0, \kappa)$. *The PSE contains* $\delta_m \sim \mathcal{UF}[-\tau, \tau]$ *and* $\gamma_m \sim \mathcal{VM}(0, \kappa)$. *Note that* $\tau \in [0, \pi/2]$ *and* $\kappa \geq 1$. *If* $\bar{\delta}_m$ *and* δ_m *are i.i.d.,* $\bar{\gamma}_m$ *and* γ_m *are i.i.d, then the upper bounds of the RP* Γ *in* (8) *can be obtained as*

$$\Gamma_{(3.10)} \leq \Gamma^{\star}_{(3.10)} \approx \left(\frac{1-b}{2}\sin(\phi_m - c)\eta + \frac{1+b}{2}\right)^2\eta^2 < \Gamma^{\star}_{(3.10)}(\phi_{\mathsf{U}}), \quad (25)$$

where $\Gamma_{(3.10)} = \left|\mathbb{E}\left\{\beta(\phi_m + \bar{\delta}_m + \bar{\gamma}_m)\exp(-\jmath(\delta_m + \gamma_m))\right\}\right|^2$, $\Gamma^{\star}_{(3.10)} = \left|\mathbb{E}\left\{\bar{\beta}(\phi_m + \bar{\delta}_m + \bar{\gamma}_m)\exp(-\jmath(\delta_m + \gamma_m))\right\}\right|^2$, *and* $\eta = \left(1 - \frac{1}{6}\tau^2 + \frac{1}{120}\tau^4\right)\rho$. $\Gamma^{\star}_{(3.10)}(\phi_{\mathsf{U}}) = \left(\frac{1-b}{2}\eta + \frac{1+b}{2}\right)^2\eta^2$.

Proof: Please see Appendix D. ∎

Figs. 16a and 16b present 3D plots of the MC and AN results for Prop. 3.10. Figs. 17a and 17b illustrate that as the RIS phase shifts approach the ends of their range, the RP under i.i.d. PEs in both the PSE and PDA cases becomes smaller than that under identical PEs, whereas this relationship reverses when the phase shifts are near the middle of their range. Therefore, when the RIS is new and its components are highly correlated (i.e., $\iota = 1$), the phase shift set $\{\phi_m\}_{m=1}^M$ should be configured near the ends of their range to achieve a higher Γ. Conversely, after long-term use with reduced correlation (i.e., $\iota = 0$), $\{\phi_m\}_{m=1}^M$ should be set close to the middle of the range.

IV. Channel Modeling and Spectral Efficiency Analysis

In this section, we first present a LoS channel model of the NF RIS-aided communication considering the PDA, the PSE,

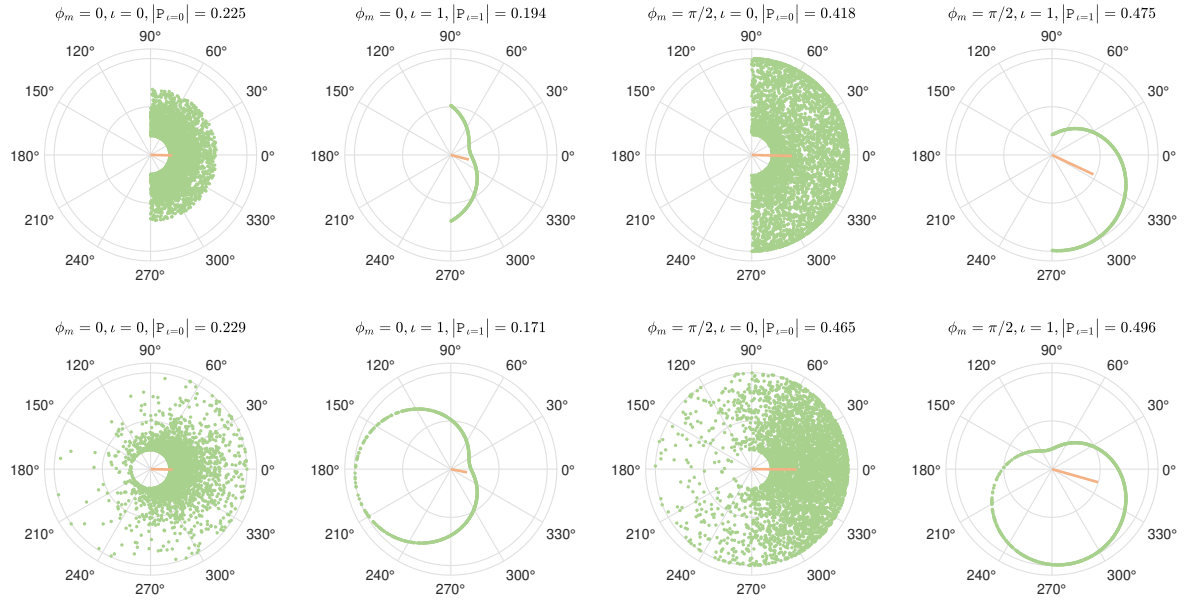

Fig. 14: Vector field distribution with $\mathcal{UF}$ and $\mathcal{VM}$ RVs to verify Remark II. Note that $\mathsf{P} = \mathsf{P}(\bar{\Delta}, \Delta)$ as Appendix B defines.

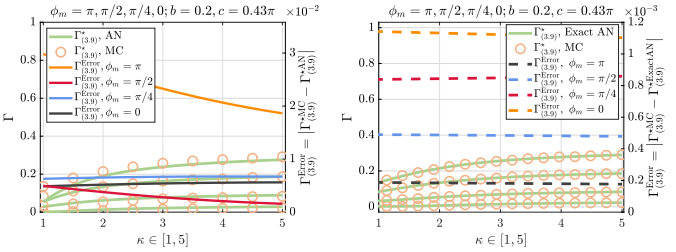

(a) Validation of $\Gamma^{\star}_{(3.9)}$. (b) Exact expression of $\Gamma^{\star}_{(3.9)}$.

Fig. 15: Validation of Prop. 3.9.

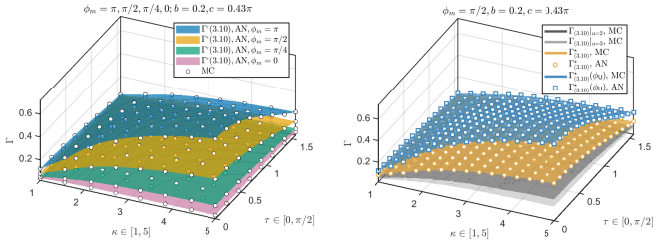

(a) Validation of $\Gamma^{\star}_{(3.10)}$. (b) Validation of Prop. 3.10.

Fig. 16: Validation of Prop. 3.10.

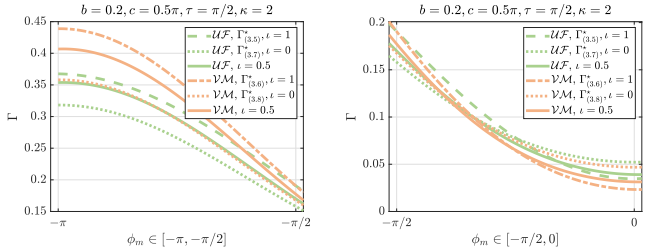

(a) $\phi_m \in [-\pi, -\pi/2]$. (b) $\phi_m \in [-\pi/2, 0]$.

Fig. 17: RP comparison under different ι.

and the PE. Subsequently, a tight closed-form SE upper bound for the model is derived.

A. Line-of-Sight Channel Near-Field Modeling

Consider an RIS-aided system comprising an AP, a user, and an RIS. The transceivers both equip single isotropic antennas. The direct link is blocked, and the RIS with M pixels is a planar surface on a rectangular grid spaced d_x and d_y apart in the xoy-plane of a three-dimensional (3D) Cartesian coordinate system where o denotes the origin point, and the area and the geometric center of the RIS are respectively $d_x\sqrt{M} \times d_y\sqrt{M}$ and $[0, h_y, 0]^{\mathsf{T}}$, where h_y is the height of the RIS. Furthermore, it is assumed that the hardware structure and area of each pixel are the same, i.e., the area is $d_x d_y$. The position of the AP and the user are $D_{\mathrm{AP}} = [x_{\mathrm{AP}}, y_{\mathrm{AP}}, z_{\mathrm{AP}}]^{\mathsf{T}}$ and $D_{\mathrm{User}} = [x_{\mathrm{User}}, y_{\mathrm{User}}, z_{\mathrm{User}}]^{\mathsf{T}}$, respectively. The coordinate of the RIS is $D_{m_1 m_2} = [\Psi(m_1, d_x, \sqrt{M}), \Psi(m_2, d_y, \sqrt{M}) + h_y, 0]^{\mathsf{T}}$, where m_1 and $m_2 \in \{((\sqrt{M}+1) \bmod 2) - \lfloor \frac{\sqrt{M}}{2} \rfloor, \ldots, \lfloor \frac{\sqrt{M}}{2} \rfloor\}$, $\Psi(m_1, d_x, \sqrt{M}) = d_x(m_1 - 0.5((\sqrt{M}+1) \bmod 2))$, and $\Psi(m_2, d_y, \sqrt{M}) = d_y(m_2 - 0.5((\sqrt{M}+1) \bmod 2))$. Moreover, by using an applicable mapping function $\mathcal{M}(m_1, m_2) = m$ where $m = 1, \ldots, M$, we can replace the notation $D_{m_1 m_2}$ with $D_m = [x_m, y_m, 0]^{\mathsf{T}}$ to guarantee a more concise expression. Additionally, for the AP and the user, it is assumed that the *visibility region* [34] of the RIS always consists of total M pixels, i.e., the transceiver can observe the entire RIS.

Therefore, the distances between the AP and the m-th pixel and between the m-th pixel and the user can be respectively obtained as $d_{\mathrm{AP}\to m} = \|D_m - D_{\mathrm{AP}}\|$ and $d_{m\to\mathrm{User}} = \|D_{\mathrm{User}} - D_m\|$. Accordingly, the time delays are $\varpi_{\mathrm{AP}\to m} = d_{\mathrm{AP}\to m}/\nu$ and $\varpi_{\mathrm{m}\to\mathrm{User}} = d_{\mathrm{m}\to\mathrm{User}}/\nu$, respectively, where ν denotes the speed of light. Using *Friis transmission formula* [35], for the

m-th AP-to-pixel path g_m, we have[12]

$$\frac{P_{\mathrm{AP}\to m}}{P_{\mathrm{AP}}}=\left(\frac{\lambda}{4\pi d_{\mathrm{AP}\to m}}\right)^2 G_{\mathrm{AP}} G_{\mathrm{AP}\to m}, \tag{26}$$

where $P_{\mathrm{AP}\to m}$ is the received power of the m-th RIS pixel, which is part of the power that is emitted from the AP, i.e., P_{AP}. Besides, G_{AP} and $G_{\mathrm{AP}\to m}$ are the AP antenna gain and the m-th pixel gain from the direction of the AP. For $G_{\mathrm{AP}\to m}$, we consider a generic directional gain pattern [37], i.e., $\vartheta_{\mathrm{AP}\to m}(\theta_{\mathrm{AP}\to m},\psi_{\mathrm{AP}\to m}) = \bar{r}\cos^{2r}(\theta_{\mathrm{AP}\to m})$ if $\theta_{\mathrm{AP}\to m}\in[0,\pi/2)$ and $\psi_{\mathrm{AP}\to m}\in[0,2\pi]$, or 0 otherwise. Note that $\theta_{\mathrm{AP}\to m}=\arccos\left(\frac{z_{\mathrm{AP}}}{d_{\mathrm{AP}\to m}}\right)\in[0,\pi/2)$ and $\psi_{\mathrm{AP}\to m}=\arctan\left(\frac{y_{\mathrm{AP}}-y_m}{x_{\mathrm{AP}}-x_m}\right)\in[0,2\pi]$. Note that the directional gain pattern should be considered in the NF scenario [6], thus each pixel has its own effective aperture. Consider the law of power conservation [38], we have

$$\begin{aligned}&\int_0^{2\pi}\partial\psi_{\mathrm{AP}\to m}\int_0^{\frac{\pi}{2}}\bar{r}\cos^{2r}(\theta_{\mathrm{AP}\to m})\sin(\theta_{\mathrm{AP}\to m})\\&=\bar{r}2\pi\left[-\frac{\cos^{(2r+1)}(\theta_{\mathrm{AP}\to m})}{2r+1}\right]_0^{\frac{\pi}{2}}=\bar{r}\frac{2\pi}{2r+1}=4\pi,\end{aligned} \tag{27}$$

thus $\bar{r}=2(2r+1)$. In this paper, we assume cosine pattern, i.e., *projected aperture* [6], thus $r=\frac{1}{2}$ and $\bar{r}=4$. Consequently, $\vartheta_{\mathrm{AP}\to m}(\theta_{\mathrm{AP}\to m},\psi_{\mathrm{AP}\to m})=4\cos(\theta_{\mathrm{AP}\to m})$. Similarly, for the m-th pixel-to-user path h_m, we have

$$\frac{P_{m\to\mathrm{User}}}{P_m}=\left(\frac{\lambda}{4\pi d_{m\to\mathrm{User}}}\right)^2 G_{\mathrm{User}} G_{m\to\mathrm{User}}, \tag{28}$$

where $P_{m\to\mathrm{User}}$ is the received power of the user, which is part of the power that is emitted from the m-th RIS pixel, i.e., P_m. It is worth noting that the pixel may contain the PSE, the PDA, and the PEs, thus $P_{\mathrm{AP}\to m}\geq P_m$. Besides, G_{User} and $G_{m\to\mathrm{User}}$ are respectively the user antenna gain and the m-th pixel gain from the direction of the user, and $\vartheta_{m\to\mathrm{User}}(\theta_{m\to\mathrm{User}},\psi_{m\to\mathrm{User}})=4\cos(\theta_{m\to\mathrm{User}})$ where $\theta_{m\to\mathrm{User}}=\arccos\left(\frac{z_{\mathrm{User}}}{d_{m\to\mathrm{User}}}\right)\in[0,\frac{\pi}{2})$ and $\psi_{m\to\mathrm{User}}=\arctan\left(\frac{y_{\mathrm{User}}-y_m}{x_{\mathrm{User}}-x_m}\right)\in[0,2\pi]$. Besides, based on Fig. 2, we have $\Gamma_m=\frac{P_m}{P_{\mathrm{AP}\to m}}$, where Γ_m denotes the RP for the m-th pixel with the PSE, the PDA, and the PEs.

Therefore, the m-th end-to-end power gain from the AP to the user can be obtained as (29) in the next page, where $G_{\mathrm{AP}\to m}=\frac{4\pi}{\lambda^2}d_x d_y\vartheta_{\mathrm{AP}\to m}=\frac{16\pi}{\lambda^2}d_x d_y\cos(\theta_{\mathrm{AP}\to m})$ and $G_{m\to\mathrm{User}}=\frac{4\pi}{\lambda^2}d_x d_y\vartheta_{m\to\mathrm{User}}=\frac{16\pi}{\lambda^2}d_x d_y\cos(\theta_{m\to\mathrm{User}})$. Since the antennas in the transceiver are isotropic, then $G_{\mathrm{AP}}=G_{\mathrm{User}}=1$. Thus the m-th LoS channel of the AP-to-pixel and the pixel-to-user paths are respectively $g_m=A_{\mathrm{AP}\to m}\exp(-\jmath 2\pi f_c\varpi_{\mathrm{AP}\to m})$ and $h_m=A_{m\to\mathrm{User}}\exp(-\jmath 2\pi f_c\varpi_{m\to\mathrm{User}})$, where f_c is carrier frequency,

$$A_{\mathrm{AP}\to m}=\frac{\lambda}{4\pi d_{\mathrm{AP}\to m}}\sqrt{G_{\mathrm{AP}\to m}}, \tag{30}$$

and

$$A_{m\to\mathrm{User}}=\frac{\lambda}{4\pi d_{m\to\mathrm{User}}}\sqrt{G_{m\to\mathrm{User}}}. \tag{31}$$

Therefore, for the m-th channel, if the model is without any PEs, the PSE, or the PDA, the baseband equivalent of the received passband signal can be obtained as $g_m h_m\exp(-\jmath\phi_m)$ where $\phi_m=-2\pi f_c(\varpi_{\mathrm{AP}\to m}+\varpi_{m\to\mathrm{User}})+2k\pi$ and k is a non-negative integer. Consider the RIS with M pixels, and the PSE and the PDA coexist, then we have a total baseband equivalent channel as

$$y=hs\sqrt{P_{\mathrm{AP}}}+\omega, \tag{32}$$

where $h=\sum_m g_m\beta(\phi_m+\bar{\Delta}_m)\exp(-\jmath(\phi_m+\Delta_m))h_m$, $\bar{\Delta}_m$ and Δ_m are the PEs, s is a unit-power signal symbol, and $\omega\sim\mathcal{CN}(0,\sigma^2)$ denotes additive white Gaussian noise with the variance σ^2, then the SE at the user side is given by

$$\mathsf{SE}=\mathbb{E}\left\{\log_2\left(1+\frac{P_{\mathrm{AP}}|h|^2}{\sigma^2}\right)\right\}. \tag{33}$$

Remark III: Note that for the RIS with M pixels, Γ_m generally differ because each scatterer exhibits distinct characteristics. Consequently, the term $\beta(\phi_m+\bar{\Delta}_m)$ of h in (32) cannot be factored outside the summation, and a closed-form expression for Γ_m is generally unavailable. However, based on the last step of (8), when the number of pixels is sufficiently large (e.g., larger than 200), the RP obtained in the previous section can be used to evaluate the SE. Accordingly, in the next section, we derive the SE expression together with its lower and upper bounds.

B. Spectral Efficiency Analysis

It can be obtained that [9]

$$\mathsf{SE}=\mathbb{E}\left\{\log_2\left(1+\frac{P_{\mathrm{AP}}|h|^2}{\sigma^2}\right)\right\}\approx\log_2\left(1+\frac{P_{\mathrm{AP}}\mathbb{E}\{|h|^2\}}{\sigma^2}\right). \tag{34}$$

[12]Although spatial correlations and polarization effects can adversely impact system performance [9], these factors are primarily associated with the interval between two pixels and the RIS position [36]. As such, they are not directly related to the PE, the PSE, or the PDA, which are the focus of this study. Consequently, this paper does not delve into the implications of the spatial correlation and the polarization.

$$\frac{P_{m\to\mathrm{User}}}{P_{\mathrm{AP}}}=\overbrace{\frac{P_{\mathrm{AP}\to m}}{P_{\mathrm{AP}}}}^{|g_m|^2}\overbrace{\frac{P_m}{P_{\mathrm{AP}\to m}}}^{\Gamma_m}\overbrace{\frac{P_{m\to\mathrm{User}}}{P_m}}^{|h_m|^2}=\underbrace{\left(\frac{\lambda}{4\pi d_{\mathrm{AP}\to m}}\right)^2 G_{\mathrm{AP}} G_{\mathrm{AP}\to m}}_{A_{\mathrm{AP}\to m}^2}\Gamma_m\underbrace{\left(\frac{\lambda}{4\pi d_{m\to\mathrm{User}}}\right)^2 G_{\mathrm{User}} G_{m\to\mathrm{User}}}_{A_{m\to\mathrm{User}}^2}, \tag{29}$$

Based on (6) and recall $\phi_{\mathsf{U}} = \pi/2 + c$ and $\phi_{\mathsf{L}} = -\pi/2 + c$, we have $\mathsf{L} < \mathsf{H} < \mathsf{U}$, where

$$\begin{aligned}\mathsf{L} &= \mathbb{E}\left\{\left|\sum_{m=1}^{M} g_m \beta(\phi_{\mathsf{L}} + \Delta_m)\exp(-\jmath(\phi_m + \Delta_m))h_m\right|^2\right\} \\ &\approx \left(\sum_{m=1}^{M} A_{\mathrm{AP}\to m}\sqrt{\Gamma_{(\cdot)}(\phi_{\mathsf{L}})}A_{m\to\mathrm{User}}\right)^2 \\ &= \Gamma_{(\cdot)}(\phi_{\mathsf{L}})\left(\sum_{m=1}^{M} A_{\mathrm{AP}\to m}A_{m\to\mathrm{User}}\right)^2, \end{aligned} \tag{35}$$

$$\begin{aligned}\mathsf{H} &= \mathbb{E}\left\{\left|\sum_{m=1}^{M} g_m \beta(\phi_m + \Delta_m)\exp(-\jmath(\phi_m + \Delta_m))h_m\right|^2\right\} \\ &\approx \left(\sum_{m=1}^{M} A_{\mathrm{AP}\to m}\sqrt{\Gamma_{(\cdot)}(\phi_m)}A_{m\to\mathrm{User}}\right)^2, \end{aligned} \tag{36}$$

and

$$\begin{aligned}\mathsf{U} &= \mathbb{E}\left\{\left|\sum_{m=1}^{M} g_m \beta(\phi_{\mathsf{U}} + \Delta_m)\exp(-\jmath(\phi_m + \Delta_m))h_m\right|^2\right\} \\ &\approx \left(\sum_{m=1}^{M} A_{\mathrm{AP}\to m}\sqrt{\Gamma_{(\cdot)}(\phi_{\mathsf{U}})}A_{m\to\mathrm{User}}\right)^2 \\ &= \Gamma_{(\cdot)}(\phi_{\mathsf{U}})\left(\sum_{m=1}^{M} A_{\mathrm{AP}\to m}A_{m\to\mathrm{User}}\right)^2. \end{aligned} \tag{37}$$

Using Props. 3.1 to 3.10, we can obtain $\Gamma_{(\cdot)}(\phi_{\mathsf{L}})$ and $\Gamma_{(\cdot)}(\phi_{\mathsf{U}})$ considering different noises situations. Next, we first compute $|\sum_m A_{\mathrm{AP}\to m}A_{m\to\mathrm{User}}|^2$, then $|\sum_m A_{\mathrm{AP}\to m}\sqrt{\Gamma_{(\cdot)}}A_{m\to\mathrm{User}}|^2$ can be obtained easily. Note that $A_{\mathrm{AP}\to m}$ in (30) and $A_{m\to\mathrm{User}}$ in (31) only contain non-negative components, we have (38) in the next page. Based on *CBS inequality* [39], we have (39) in the next page, where $\mathsf{S}_m = \left((x_m - x_{\mathrm{AP}})^2 + (y_m - y_{\mathrm{AP}})^2 + z_{\mathrm{AP}}^2\right)^{-\frac{3}{2}}$, $\mathsf{T}_m = \left((x_{\mathrm{User}} - x_m)^2 + (y_{\mathrm{User}} - y_m)^2 + z_{\mathrm{User}}^2\right)^{-\frac{3}{2}}$, $\mathsf{S}_m^{\mathrm{Upper}}$ and $\mathsf{T}_m^{\mathrm{Upper}}$ are defined as the right-hand sides of the first rows of (40) and (42), respectively. The equality holds when $\sqrt{\mathsf{S}_m}$ and $\sqrt{\mathsf{T}_m}$ are proportional. Note that the area of each pixel is $d_x d_y$, instead of an ideal point. Therefore, by using *Riemann sums* [39], we have

$$\begin{aligned}\mathsf{S}_m^{\mathrm{Upper}} &= \int_{x_m-\frac{d_x}{2}}^{x_m+\frac{d_x}{2}}\int_{y_m-\frac{d_y}{2}}^{y_m+\frac{d_y}{2}} \mathsf{S}_m \partial x_m \partial y_m \\ &= \mathsf{Q}(t_2, t_4, z_{\mathrm{AP}}) - \mathsf{Q}(t_1, t_4, z_{\mathrm{AP}}) \\ &\quad - \mathsf{Q}(t_2, t_3, z_{\mathrm{AP}}) + \mathsf{Q}(t_1, t_3, z_{\mathrm{AP}}), \end{aligned} \tag{40}$$

where $\mathsf{Q}(s_1, s_2, z)$ is defined as

$$\mathsf{Q}(s_1, s_2, z) = \frac{1}{z}\arctan\left(\frac{s_1 s_2}{z\sqrt{s_1^2 + s_2^2 + z^2}}\right), \tag{41}$$

and $t_1 = x_m - \frac{d_x}{2} - x_{\mathrm{AP}}$, $t_2 = x_m + \frac{d_x}{2} - x_{\mathrm{AP}}$, $t_3 = y_m - \frac{d_y}{2} - y_{\mathrm{AP}}$, and $t_4 = y_m + \frac{d_y}{2} - y_{\mathrm{AP}}$. Similarly, we also have

$$\begin{aligned}\mathsf{T}_m^{\mathrm{Upper}} &= \int_{x_m-\frac{d_x}{2}}^{x_m+\frac{d_x}{2}}\int_{y_m-\frac{d_y}{2}}^{y_m+\frac{d_y}{2}} \mathsf{T}_m \partial x_m \partial y_m \\ &= \mathsf{Q}(t_6, t_8, z_{\mathrm{User}}) - \mathsf{Q}(t_5, t_8, z_{\mathrm{User}}) \\ &\quad - \mathsf{Q}(t_6, t_7, z_{\mathrm{User}}) + \mathsf{Q}(t_5, t_7, z_{\mathrm{User}}), \end{aligned} \tag{42}$$

where $t_5 = x_m - \frac{d_x}{2} - x_{\mathrm{User}}$, $t_6 = x_m + \frac{d_x}{2} - x_{\mathrm{User}}$, $t_7 = y_m - \frac{d_y}{2} - y_{\mathrm{User}}$, and $t_8 = y_m + \frac{d_y}{2} - y_{\mathrm{User}}$. For the proofs of (40) and (42), please see Appendix E. Consequently, we have

$$\left(\sum_{m=1}^{M} A_{\mathrm{AP}\to m}A_{m\to\mathrm{User}}\right)^2 \le \frac{z_{\mathrm{AP}} z_{\mathrm{User}}}{\pi^2}\sum_{m=1}^{M}\mathsf{S}_m^{\mathrm{Upper}}\sum_{m=1}^{M}\mathsf{T}_m^{\mathrm{Upper}}, \tag{43}$$

and the equality holds when the pixel area $d_x d_y$ is small enough. Therefore, we have

$$\mathsf{L}^{\mathrm{Upper}} = \Gamma_{(\cdot)}(\phi_{\mathsf{L}})\frac{z_{\mathrm{AP}} z_{\mathrm{User}}}{\pi^2}\sum_{m=1}^{M}\mathsf{S}_m^{\mathrm{Upper}}\sum_{m=1}^{M}\mathsf{T}_m^{\mathrm{Upper}} \tag{44}$$

and

$$\mathsf{U}^{\mathrm{Upper}} = \Gamma_{(\cdot)}(\phi_{\mathsf{U}})\frac{z_{\mathrm{AP}} z_{\mathrm{User}}}{\pi^2}\sum_{m=1}^{M}\mathsf{S}_m^{\mathrm{Upper}}\sum_{m=1}^{M}\mathsf{T}_m^{\mathrm{Upper}}. \tag{45}$$

Besides, using the results above, we can obtain H as

$$\begin{aligned}\mathsf{H} &\approx \left(\sum_{m=1}^{M} A_{\mathrm{AP}\to m}\sqrt{\Gamma_{(\cdot)}(\phi_m)}A_{m\to\mathrm{User}}\right)^2 \\ &\le \frac{z_{\mathrm{AP}} z_{\mathrm{User}}}{\pi^2}\sum_{m=1}^{M}\sqrt{\Gamma_{(\cdot)}(\phi_m)}\mathsf{S}_m^{\mathrm{Upper}}\sum_{m=1}^{M}\mathsf{T}_m^{\mathrm{Upper}} \\ &= \mathsf{H}^{\mathrm{Upper}}. \end{aligned} \tag{46}$$

Finally, we have a theorem as follows.

Theorem 1 (Lower and upper bounds of the SE): *It can be obtained that*

$$\underbrace{\mathsf{SE}_{\mathsf{L}} \overset{(i)}{\le} \mathsf{SE}_{\mathsf{L}}^{\mathrm{Upper}}}_{\text{Contains } \phi_{\mathsf{L}}} < \underbrace{\mathsf{SE} \overset{(ii)}{\le} \mathsf{SE}^{\mathrm{Upper}}}_{\text{Contains } \phi_m} < \underbrace{\mathsf{SE}_{\mathsf{U}} \overset{(iii)}{\le} \mathsf{SE}_{\mathsf{U}}^{\mathrm{Upper}}}_{\text{Contains } \phi_{\mathsf{U}}}, \tag{47}$$

where $\mathsf{SE}_{\mathsf{L}} = \log_2\left(1 + \frac{P_{\mathrm{AP}}\mathsf{L}}{\sigma^2}\right)$, $\mathsf{SE}_{\mathsf{L}}^{\mathrm{Upper}} = \log_2\left(1 + \frac{P_{\mathrm{AP}}\mathsf{L}^{\mathrm{Upper}}}{\sigma^2}\right)$, $\mathsf{SE} \approx \log_2\left(1 + \frac{P_{\mathrm{AP}}\mathsf{H}}{\sigma^2}\right)$, $\mathsf{SE}^{\mathrm{Upper}} \approx \log_2\left(1 + \frac{P_{\mathrm{AP}}\mathsf{H}^{\mathrm{Upper}}}{\sigma^2}\right)$, $\mathsf{SE}_{\mathsf{U}} =$

$$\left|\sum_{m=1}^{M} A_{\mathrm{AP}\to m}A_{m\to\mathrm{User}}\right|^2 = \frac{z_{\mathrm{AP}} z_{\mathrm{User}}}{\pi^2}\left(\sum_{m=1}^{M}\frac{d_x d_y}{(d_{\mathrm{AP}\to m}d_{m\to\mathrm{User}})^{\frac{3}{2}}}\right)^2 = \frac{d_x^2 d_y^2 z_{\mathrm{AP}} z_{\mathrm{User}}}{\pi^2}\left(\sum_{m=1}^{M}\frac{1}{(d_{\mathrm{AP}\to m}d_{m\to\mathrm{User}})^{\frac{3}{2}}}\right)^2 \tag{38}$$

$$\left|\sum_{m=1}^{M} A_{\mathrm{AP}\to m}A_{m\to\mathrm{User}}\right|^2 \le \frac{d_x^2 d_y^2 z_{\mathrm{AP}} z_{\mathrm{User}}}{\pi^2}\sum_{m=1}^{M}\mathsf{S}_m\sum_{m=1}^{M}\mathsf{T}_m \le \frac{z_{\mathrm{AP}} z_{\mathrm{User}}}{\pi^2}\sum_{m=1}^{M}\mathsf{S}_m^{\mathrm{Upper}}\sum_{m=1}^{M}\mathsf{T}_m^{\mathrm{Upper}} \tag{39}$$

$\log_2\left(1+\frac{P_{\mathrm{AP}}\mathsf{U}}{\sigma^2}\right)$, *and* $\mathsf{SE}_{\mathsf{U}}^{\mathrm{Upper}}=\log_2\left(1+\frac{P_{\mathrm{AP}}\mathsf{U}^{\mathrm{Upper}}}{\sigma^2}\right)$. *Note that* (i), (ii) *and* (iii) *are satisfied with equal measure when* d_xd_y *is sufficiently small. Besides,* L, $\mathsf{L}^{\mathrm{Upper}}$, U, $\mathsf{U}^{\mathrm{Upper}}$, H, *and* $\mathsf{H}^{\mathrm{Upper}}$ *are defined in* (35), (44), (37), (45), *and* (46) *respectively.*

Proof: Consider (35), (44), (37), (45), and (46), we have $\mathsf{SE}_{\mathsf{L}}\le\mathsf{SE}_{\mathsf{L}}^{\mathrm{Upper}}$, $\mathsf{SE}_{\mathsf{U}}\le\mathsf{SE}_{\mathsf{U}}^{\mathrm{Upper}}$ and $\mathsf{SE}\le\mathsf{SE}^{\mathrm{Upper}}$, where the equality holds when d_xd_y is small enough. $\mathsf{SE}_{\mathsf{L}}^{\mathrm{Upper}}<\mathsf{SE}$ and $\mathsf{SE}^{\mathrm{Upper}}<\mathsf{SE}_{\mathsf{U}}$ are also obvious. ■

V. Numerical Evaluations and Discussions

In this section, we present numerical results to evaluate the AN results in Secs. II, III, and IV. In particular, $D_{\mathrm{AP}}=[-20,15,8]^{\mathsf{T}}$ m, $D_{\mathrm{User}}=[20,1.5,8]^{\mathsf{T}}$ m, the center of RIS with $h_y=10$ m is $D_m=[0,10,0]^{\mathsf{T}}$. Besides, $a=1$, $b=0.2$, $c=0.43\pi$, $P_{\mathrm{AP}}=20$ dBm, $\sigma^2=-80$ dBm, and $f_c=2.4$ GHz, the pixel number[13] $M=200^2$, the MC realization number is 5000. Lastly, to evaluate the most severe hardware impairment scenario, we perform system-level simulations using $\Gamma^{\star}_{(3.10)}$ as the RP expression. Three simulation scenarios are considered for validation. To cover a wider range of boundary conditions, the position coordinates of the RIS, the AP, and the user are allowed to take negative values.

A. When the RIS is Fixed

We first evaluate the system performance when the RIS is located in the middle of the AP and the user, i.e., $D_m=[0,10,0]^{\mathsf{T}}$.

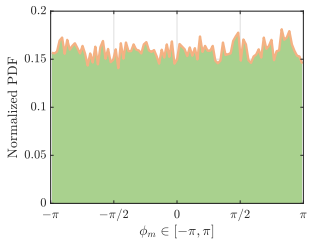

(a) The empirical PDF of ϕ_m.

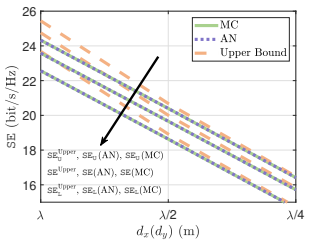

(b) SE on different pixel sizes.

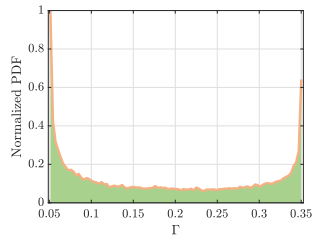

(c) The empirical PDF of Γ.

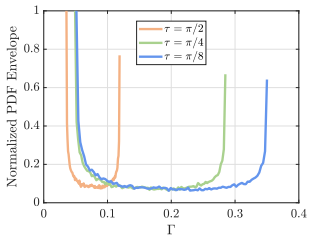

(d) The PDF of Γ for different τ.

Fig. 18: System performance when the RIS is fixed.

From Fig. 18a, it can be observed that the empirical PDF of ϕ_m distributed over $[-\pi,\pi]$, this aligns with our assumption in the last step of (8). Fig. 18b shows that decreasing the area of the pixel (i.e., d_xd_y) would diminish the SE. Besides, the upper bound of the SE would approach the simulated results, i.e., (47) becomes $\mathsf{SE}_{\mathsf{L}}=\mathsf{SE}_{\mathsf{L}}^{\mathrm{Upper}}>\mathsf{SE}=\mathsf{SE}^{\mathrm{Upper}}>\mathsf{SE}_{\mathsf{U}}=\mathsf{SE}_{\mathsf{U}}^{\mathrm{Upper}}$. This is because the area and the center point of the pixel can be regarded as the same when $d_x=d_y\le\frac{\lambda}{4}$, and shows the correctness of Theorem 1. Although $\phi_m\sim\mathcal{UF}[-\pi,\pi]$, Fig. 18c shows Γ exhibits a U-shaped distribution. This is caused by the nonlinear feature of the PDA. Fig. 18d illustrates the PDFs for different values of τ, showing broader distributions and reduced peaks as τ increases, while a similar trend can be observed when κ decreases.

[13]While $M=500$ is sufficient based on Sec.III, we choose a larger value to obtain more compelling MC results.

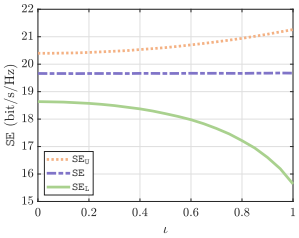

(a) SE for different ι.

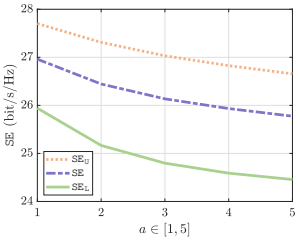

(b) SE for different a.

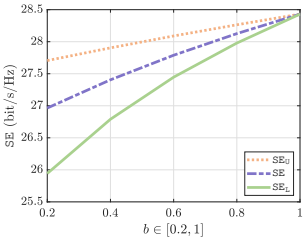

(c) SE for different b.

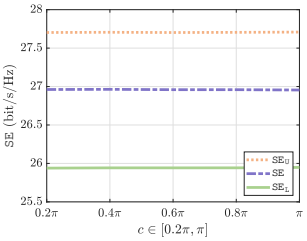

(d) SE for different c.

Fig. 19: SE performance for different parameters.

Fig. 19 illustrates the SE for different ι, a, b, and c. As expected, when $\phi_m=\phi_{\mathsf{L}}$, the SE decreases as ι increases, and vice versa. This is consistent with Figs. 4 and 13. Moreover, SE increases with smaller a and decreases with larger b. In contrast, c has negligible impact on SE because it only shifts the PDA curve. This result is in good agreement with Fig. 3f.

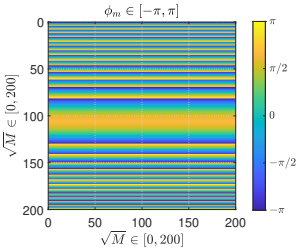

(a) Heatmap of ϕ_m.

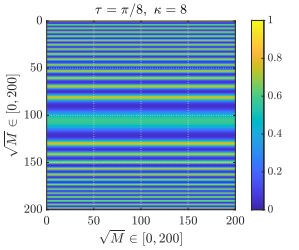

(b) $\tau=\pi/8$ and $\kappa=8$.

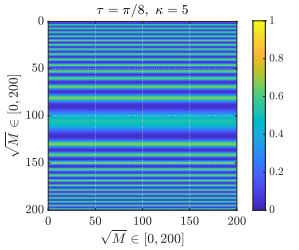

(c) $\tau=\pi/8$ and $\kappa=5$.

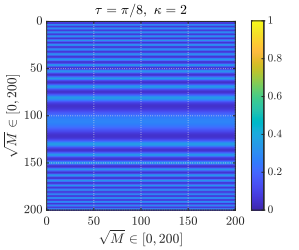

(d) $\tau=\pi/8$ and $\kappa=2$.

Fig. 20: Heatmaps of ϕ and Γ when the RIS is fixed.

Fig. 20 visualizes ϕ_m and Γ using heatmaps. With $\tau = \pi/8$ and $\kappa = 2, 5, 8$, we can see that ϕ_m is approximately uniform over $[-\pi, \pi]$. Besides, as κ decreases, phase concentration decreases and both the peak and span of high Γ regions shrink, with weak sensitivity to M. These trends align with the SE improving as noise decreases. In addition, it is worth emphasizing that the pattern of the phase distribution is related to the positions of the RIS, AP, and user, since the RIS phases are designed based on location information rather than instantaneous channel state information.

B. When the RIS Moves along x-axis

We further consider a slow movement of the RIS from a position near the AP toward the user. The RIS center is set to $[x_{\text{RIS}}, 10, 0]^{\mathsf{T}}$ m with $x_{\text{RIS}} \in [-8, 8]$ m, and the Doppler effect is neglected.

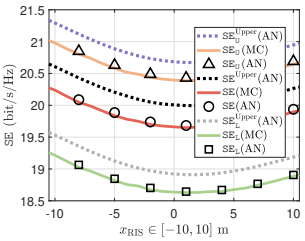

(a) Validation of Theorem 1.

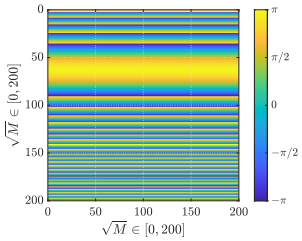

(b) Heatmap of ϕ_m, $x_{\text{RIS}} = 8$.

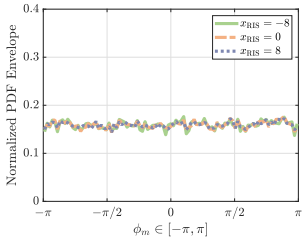

(c) The empirical PDF of ϕ_m.

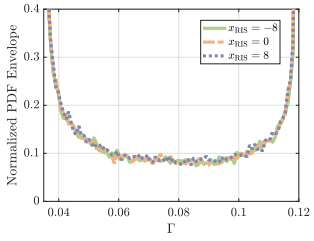

(d) The empirical PDF of Γ.

Fig. 21: System performance for the RIS x-axis movement.

Fig. 21a verifies the correctness of Theorem 1 in Sec. IV, as MC and AN results match well. Moreover, SE first decreases and then increases, as the RIS performs worst when it is deployed in the middle of the AP and the user [26]. Fig. 21b shows heatmap of ϕ_m when $x_{\text{RIS}} = 8$. Compared to Fig. 20a with $x_{\text{RIS}} = 0$, although the overall periodic pattern remains similar, slight displacements in the central region and phase gradient occur, indicating that the horizontal shift of the RIS introduces spatial variations in the phase distribution. Figs. 21c and 21d demonstrate that the statistical distributions of ϕ_m and Γ are independent of the RIS's position, as the curves for different x_{RIS} are nearly identical.

C. When the RIS Moves along z-axis

Next, we consider the RIS center is set to $[0, 10, z_{\text{RIS}}]^{\mathsf{T}}$ m with $z_{\text{RIS}} \in [-20, 10]$ m, and the Doppler effect is neglected. Fig. 22a illustrates that as z_{RIS} increases, the SE first rises due to the reduced propagation distance, but then falls as the projected aperture diminishes to nearly zero. However,

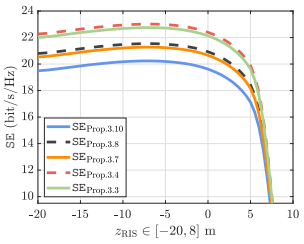

(a) SE with different Γ.

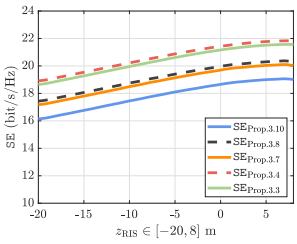

(b) Without project aperture.

Fig. 22: System performance for the RIS z-axis movement.

as shown in Fig. 22b, without the projected aperture, the SE is simply inversely proportional to the distance between the transmitter and receiver. Besides, $\mathsf{SE}_{\text{Prop.3.10}}$ is smallest, as expected.

D. Optimal Phase Feasible Set Comparison

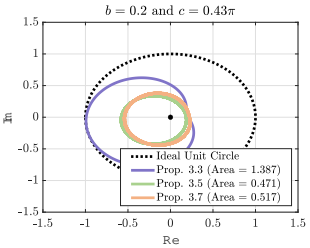

(a) Props. 3.3, 3.5, and 3.7.

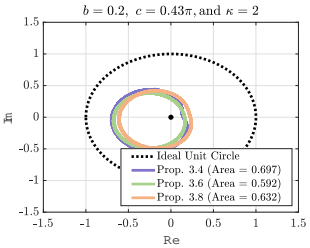

(b) Props. 3.4, 3.6, and 3.8.

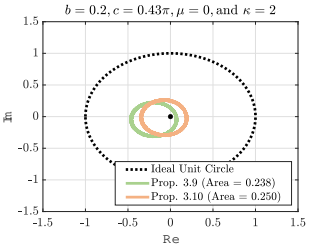

(c) Props. 3.9 and 3.10.

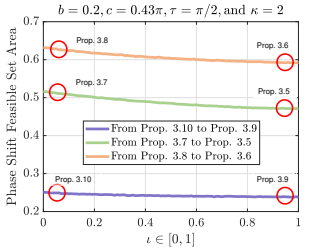

(d) Feasible set areas vs. ι.

Fig. 23: Feasible set and areas.

Figs. 23 show the feasible sets for designed RIS phases in the complex plane and their corresponding areas for the different propositions in Sec. III. As expected, greater uncertainties lead to smaller feasible set areas. Moreover, the areas and ι are inversely related. This suggests that RIS designs should be optimized to minimize noise coupling. Specifically, during the initial deployment of the RIS (i.e., $\iota = 1$), an optimization constraint can be formulated to ensure that the optimal phase remains close to the phase boundaries. However, after prolonged operation (i.e., $\iota = 0$), this constraint should be reformulated to keep the optimal phase near the middle of the phase range.

VI. Conclusions and Future Work

This paper has investigated the impact of mutual coupling and hardware imperfections in the RIS-aided system. A practical reflection framework of the RIS pixel has been

established by incorporating the PSE and the PDA, and four unified models have been proposed to characterize phase and amplitude distortions. A new metric, i.e., the RP, with asymptotic convergence has been derived to quantify reflection performance, providing a rigorous theoretical basis for system analysis. Moreover, a general NF LoS channel model has been developed, and analytical upper and lower bounds on the SE have been obtained. The results have demonstrated that the interplay between the PSE and the PDA significantly affects the RIS response.

Future work will focus on RIS phase optimization considering the coupling between the PDA and PE. For active RISs, where the PDA is more complex [40], it is also important to investigate imperfections in the relationship between the PDA and the PE of each active pixel. Another research direction is how to quantitatively characterize the phase and amplitude of an RIS pixel as it transitions from fully coupled to fully independent, which, based on known results, is closely related to hardware aging that occurs over time during operation [17]. Furthermore, we will extend these studies to multiuser scenarios to analyze the impact of the coupling on beamforming and interference control.

Appendix A
Proof of Proposition 3.2

We study $|\mathbb{E}\{\beta \exp(-\jmath\gamma_m)\}|^2$ where $\gamma_m \sim \mathcal{VM}(0,\kappa)$. Since $\mathbb{E}\{\beta \exp(-\jmath\gamma_m)\} = \beta\mathbb{E}\{\exp(\jmath\gamma_m)\}$, then we have

$$\begin{aligned}\mathbb{E}\{\exp(\jmath\gamma_m)\} &= \int_{-\pi}^{\pi} \exp(\jmath\gamma_m) f_\kappa(\gamma_m)\partial\gamma_m \\ &= \int_{-\pi}^{\pi} \exp(\jmath\gamma_m)\frac{\exp(\kappa\cos(\gamma_m))}{2\pi I_0(\kappa)}\partial\gamma_m \\ &= \frac{1}{2\pi I_0(\kappa)}\int_{-\pi}^{\pi}\exp(\jmath\gamma_m+\kappa\cos(\gamma_m))\partial\gamma_m \\ &= \frac{\frac{1}{2\pi}\int_{-\pi}^{\pi}\exp(\jmath\gamma_m+\kappa\cos(\gamma_m))\partial\gamma_m}{I_0(\kappa)}. \end{aligned} \quad (48)$$

Note that $I_n(\kappa) = \jmath^{-n}J_n(\jmath\kappa) = \jmath^{-n}\frac{1}{2\pi}\int_{-\pi}^{\pi}\exp(\jmath n\gamma_m + \kappa\sin(\gamma_m))\partial\gamma_m$, where J_n is the Bessel function of the first kind of order n. Let $n = 1$, then $I_1(\kappa) = \frac{1}{2\pi}\int_{-\pi}^{\pi}\exp(\jmath\gamma_m + \kappa\cos(\gamma_m))\partial\gamma_m$. Thus we have $\mathbb{E}\{\exp(-\jmath\gamma_m)\} = \mathbb{E}\{\exp(\jmath\gamma_m)\} = I_1(\kappa)/I_0(\kappa)$. Since the power series expansion of $I_n(\kappa)$ is [31]

$$I_n(\kappa) = \sum_{r=0}^{\infty}\frac{1}{r!\,(n+r)!}\left(\frac{\kappa}{2}\right)^{n+2r}, \quad (49)$$

and after some manipulations, $\rho = I_1(\kappa)/I_0(\kappa)$ can be obtained as (12). Besides, for small κ, let $\frac{\partial\rho^2}{\partial x} \geq 0$, we have $\kappa \in [-2.6,-1.81]\cup[0,1.81]$. For large κ, let $\frac{\partial\rho^2}{\partial x} \geq 0$, we have $\kappa \in (-\infty,0)\cup[0.83,+\infty)$. For small κ, we have $\kappa \in [1,1.6] \subset [0,1.81]$; for large κ, we have $\kappa \in [1.6,+\infty) \subset [0.83,+\infty)$, thus we finish the proof.

Appendix B
Proof of $\Gamma(0)|_{\iota=0} > \Gamma(0)|_{\iota=1}$ in Remark II

Let $\phi_m = 0$, then we have $\Gamma(0) = |\mathbb{E}\{\beta(\bar{\Delta})\exp(-\jmath\Delta)\}|^2 = (\mathbb{E}\{\beta(\bar{\Delta})\cos(\Delta)\})^2 + (\mathbb{E}\{\beta(\bar{\Delta})\sin(\Delta)\})^2$. Since $\mathcal{UF}$ and zero-mean $\mathcal{VM}$ distributions are all symmetry, $\mathbb{E}\{\sin(\Delta)\} = \mathbb{E}\{\sin(\bar{\Delta})\} = 0$, and $\mathbb{E}\{\beta(\bar{\Delta})\sin(\Delta)\} \approx 0$. So we have $\Gamma(0) = (\mathbb{E}\{\beta(\bar{\Delta})\cos(\Delta)\})^2 = (\mathsf{P}(\bar{\Delta},\Delta))^2$. Therefore, $\mathsf{P}(\bar{\Delta},\Delta) = \mathbb{E}\{\beta(\bar{\Delta})\cos(\Delta)\} = \mathbb{E}\{\beta(\bar{\Delta})\}\mathbb{E}\{\cos(\Delta)\} + \mathsf{Cov}(\beta(\bar{\Delta}),\cos(\Delta))$. Consequently, when $\iota = 0$, $\bar{\Delta}$ and Δ are i.i.d., $\mathsf{Cov}(\beta(\bar{\Delta}),\cos(\Delta)) = 0$, so $\Gamma(0)|_{\iota=0} = (\mathsf{P}(\bar{\Delta},\Delta)|_{\iota=0})^2 = (\mathbb{E}\{\beta(\bar{\Delta})\}\mathbb{E}\{\cos(\Delta)\})^2$. Similarly, when $\iota = 1$, $\bar{\Delta} = \Delta$, $\Gamma(0)|_{\iota=1} = (\mathsf{P}(\bar{\Delta},\Delta)|_{\iota=1})^2 = (\mathbb{E}\{\beta(\bar{\Delta})\}\mathbb{E}\{\cos(\Delta)\} + \mathsf{Cov}(\beta(\bar{\Delta}),\cos(\Delta)))^2$. Now, the target is to show $\mathsf{Cov}(\beta(\bar{\Delta}),\cos(\Delta)) = \mathsf{Cov}(\beta(\Delta),\cos(\Delta)) < 0$.

Consider Taylor expansion $\beta(\Delta) = \beta(0) + \frac{\partial\beta}{\partial\Delta}|_{\Delta=0}\Delta + \frac{1}{2}\frac{\partial^2\beta}{\partial\Delta^2}|_{\Delta=0}\Delta^2 + \mathcal{O}(\Delta^3)$ and $\cos(\Delta) = 1 - \frac{1}{2}\Delta^2 + \mathcal{O}(\Delta^4)$, we can obtain that $\mathsf{Cov}(\beta(\Delta),\cos(\Delta)) \approx -\frac{1}{4}\frac{\partial^2\beta}{\partial\Delta^2}|_{\Delta=0}\mathsf{Var}(\Delta^2)$. Note that $\frac{\partial^2\beta}{\partial\Delta^2}|_{\Delta=0} = \frac{1-b}{2}\sin(c) > 0$ when $c \in (0,\pi/2]$ and $b \in (0,1)$. Besides, $\mathsf{Var}(\Delta^2) > 0$, we then finish the proof.

Appendix C
Proof of Proposition 3.9

Note that $\sin(\phi_m - c + \delta_m + \gamma_m)\exp(-\jmath\delta)\exp(-\jmath\gamma_m) = \sin(\phi_m - c)\cos(\delta_m)\cos(\gamma_m)\exp(-\jmath\delta_m)\exp(-\jmath\gamma_m) + \cos(\phi_m - c)\sin(\delta_m)\cos(\gamma_m)\exp(-\jmath\delta_m)\exp(-\jmath\gamma_m) + \cos(\phi_m - c)\cos(\delta_m)\sin(\gamma_m)\exp(-\jmath\delta_m)\exp(-\jmath\gamma_m) - \sin(\phi_m - c)\sin(\delta_m)\sin(\gamma_m)\exp(-\jmath\delta_m)\exp(-\jmath\gamma_m)$, thus $\mathbb{E}\{\sin(\phi_m - c + \delta_m + \gamma_m)\exp(-\jmath\delta_m)\exp(-\jmath\gamma_m)\} = \sin(\phi_m - c)\mathbb{E}\{\cos(\delta_m)\exp(-\jmath\delta_m)\}\mathbb{E}\{\cos(\gamma_m)\exp(-\jmath\gamma_m)\} + \cos(\phi_m - c)\mathbb{E}\{\sin(\delta_m)\exp(-\jmath\delta_m)\}\mathbb{E}\{\cos(\gamma_m)\exp(-\jmath\gamma_m)\} + \cos(\phi_m - c)\mathbb{E}\{\cos(\delta_m)\exp(-\jmath\delta_m)\}\mathbb{E}\{\sin(\gamma_m)\exp(-\jmath\gamma_m)\} - \sin(\phi_m - c)\mathbb{E}\{\sin(\delta_m)\exp(-\jmath\delta_m)\}\mathbb{E}\{\sin(\gamma_m)\exp(-\jmath\gamma_m)\}$. Considering $\mathbb{E}\{\cos(\delta_m)\exp(-\jmath\delta_m)\} = 1 - \frac{\tau^2}{3} + \frac{\tau^4}{15} - \frac{2\tau^6}{315} + \mathcal{O}(\tau^8)$, $\mathbb{E}\{\cos(\gamma_m)\exp(-\jmath\gamma_m)\} = 1 - \frac{1}{2\kappa} - \frac{1}{8\kappa^2} - \frac{1}{16\kappa^3} + \mathcal{O}(\kappa^{-4})$, $\mathbb{E}\{\sin(\delta_m)\exp(-\jmath\delta_m)\} = -\jmath\left(\frac{\tau^2}{3} - \frac{\tau^4}{15} + \frac{2\tau^6}{315} + \mathcal{O}(\tau^8)\right)$, and $\mathbb{E}\{\sin(\gamma_m)\exp(-\jmath\gamma_m)\} = -\jmath\left(\frac{1}{2\kappa} + \frac{1}{8\kappa^2} + \frac{1}{16\kappa^3} + \mathcal{O}(\kappa^{-4})\right)$, the proof is completed.

Appendix D
Proof of Proposition 3.10

Note that $\sin(\phi_m - c + \bar{\delta}_m + \bar{\gamma}_m) = \big(\sin(\phi_m - c)\cos(\bar{\delta}_m) + \cos(\phi_m - c)\sin(\bar{\delta}_m)\big)\cos(\bar{\gamma}_m) + \big(\cos(\phi_m - c)\cos(\bar{\delta}_m) - \sin(\phi_m - c)\sin(\bar{\delta}_m)\big)\sin(\bar{\gamma}_m)$, $\mathbb{E}\{\sin(\bar{\gamma}_m)\} = \mathbb{E}\{\sin(\gamma_m)\} = \mathbb{E}\{\sin(\bar{\delta}_m)\} = \mathbb{E}\{\sin(\delta_m)\} = 0$, $\mathbb{E}\{\cos(\bar{\gamma}_m)\} = \mathbb{E}\{\cos(\gamma_m)\} = \rho$, and $\mathbb{E}\{\cos(\bar{\delta}_m)\} = \mathbb{E}\{\cos(\delta_m)\} \approx 1 - \frac{1}{6}\tau^2 + \frac{1}{120}\tau^4$, then the proof is completed.

Appendix E
Proofs of (40) and (42)

First, we have

$$\begin{aligned}\mathsf{S}_m^{\text{Upper}} &= \int_{x_m-\frac{\lambda}{4}}^{x_m+\frac{\lambda}{4}}\int_{y_m-\frac{\lambda}{4}}^{y_m+\frac{\lambda}{4}}\mathsf{S}_m\partial x_m\partial y_m \\ &= \int_{x_m-\frac{\lambda}{4}}^{x_m+\frac{\lambda}{4}}\int_{y_m-\frac{\lambda}{4}}^{y_m+\frac{\lambda}{4}}\frac{\partial x_m\partial y_m}{\left((x_m-x_{\text{AP}})^2+(y_m-y_{\text{AP}})^2+z_{\text{AP}}^2\right)^{\frac{3}{2}}}. \end{aligned} \quad (50)$$

Let $x_m - x_{\mathrm{AP}} = \mathsf{v}_m$, $y_m - y_{\mathrm{AP}} = \mathsf{w}_m$, then we have

$$\begin{aligned}
\mathsf{S}_m^{\mathrm{Upper}} &= \int_{x_m-\frac{\lambda}{4}}^{x_m+\frac{\lambda}{4}} \int_{y_m-\frac{\lambda}{4}}^{y_m+\frac{\lambda}{4}} \mathsf{S}_m \partial x_m \partial y_m \\
&= \int_{x_m-\frac{\lambda}{4}-x_{\mathrm{AP}}}^{x_m+\frac{\lambda}{4}-x_{\mathrm{AP}}} \int_{y_m-\frac{\lambda}{4}-y_{\mathrm{AP}}}^{y_m+\frac{\lambda}{4}-y_{\mathrm{AP}}} \frac{\partial \mathsf{v}_m \partial \mathsf{w}_m}{\left(\mathsf{v}_m^2+\mathsf{w}_m^2+z_{\mathrm{AP}}^2\right)^{\frac{3}{2}}} \\
&\overset{(i)}{=} \int_{t_1}^{t_2} \left[\frac{\mathsf{w}_m}{\left(\mathsf{v}_m^2+z_{\mathrm{AP}}^2\right)\sqrt{\mathsf{v}_m^2+\mathsf{w}_m^2+z_{\mathrm{AP}}^2}} \right]_{t_3}^{t_4} \partial \mathsf{v}_m \\
&\overset{(ii)}{=} \mathsf{Q}(t_2,t_4,z_{\mathrm{AP}}) - \mathsf{Q}(t_1,t_4,z_{\mathrm{AP}}) \\
&\quad - \mathsf{Q}(t_2,t_3,z_{\mathrm{AP}}) + \mathsf{Q}(t_1,t_3,z_{\mathrm{AP}}),
\end{aligned} \tag{51}$$

where $\mathsf{Q}(s_1,s_2,z)$ is

$$\mathsf{Q}(s_1,s_2,z) = \frac{1}{z}\arctan\left(\frac{s_1 s_2}{z\sqrt{s_1^2+s_2^2+z^2}}\right), \tag{52}$$

and $t_1 = x_m - \frac{\lambda}{4} - x_{\mathrm{AP}}$, $t_2 = x_m + \frac{\lambda}{4} - x_{\mathrm{AP}}$, $t_3 = y_m - \frac{\lambda}{4} - y_{\mathrm{AP}}$, and $t_4 = y_m + \frac{\lambda}{4} - y_{\mathrm{AP}}$. Besides, (i) uses $\int \frac{\partial \mathsf{v}}{(\mathsf{v}^2+\mathsf{u})^{\frac{3}{2}}} = \frac{\mathsf{v}}{\mathsf{u}\sqrt{\mathsf{v}^2+\mathsf{u}}}$ [39] and the constant term is ignored, (ii) uses $\int \frac{\mathsf{u}\partial \mathsf{v}}{(\mathsf{v}^2+\mathsf{w})\sqrt{\mathsf{v}^2+\mathsf{u}+\mathsf{w}}} = \frac{1}{\sqrt{\mathsf{w}}}\arctan\left(\frac{\sqrt{\mathsf{u}}\mathsf{v}}{\sqrt{\mathsf{w}}\sqrt{\mathsf{v}^2+\mathsf{u}+\mathsf{w}}}\right)$ [39] and the constant term is ignored. Thus (40) is obtained. Similarly, let $t_5 = x_m - \frac{\lambda}{4} - x_{\mathrm{User}}$, $t_6 = x_m + \frac{\lambda}{4} - x_{\mathrm{User}}$, $t_7 = y_m - \frac{\lambda}{4} - y_{\mathrm{User}}$, and $t_8 = y_m + \frac{\lambda}{4} - y_{\mathrm{User}}$, then we have $\mathsf{T}_m^{\mathrm{Upper}} = \mathsf{Q}(t_6,t_8,z_{\mathrm{User}}) - \mathsf{Q}(t_5,t_8,z_{\mathrm{User}}) - \mathsf{Q}(t_6,t_7,z_{\mathrm{User}}) + \mathsf{Q}(t_5,t_7,z_{\mathrm{User}})$. Therefore, (42) is achieved, concluding the proof.

REFERENCES

[1] K. Wang *et al.*, "How Phase Errors Influence Phase-Dependent Amplitudes in Near-Field RISs?" in *2024 IEEE 100th Vehicular Technology Conference (VTC2024-Fall)*, 2024, pp. 1–6.

[2] E. Björnson *et al.*, "Reconfigurable intelligent surfaces: Three myths and two critical questions," *IEEE Commun. Mag.*, vol. 58, no. 12, pp. 90–96, 2020.

[3] Q. Wu *et al.*, "Intelligent reflecting surface enhanced wireless network via joint active and passive beamforming," *IEEE Trans. Wireless Commun.*, vol. 18, no. 11, pp. 5394–5409, 2019.

[4] C. Huang *et al.*, "Reconfigurable intelligent surfaces for energy efficiency in wireless communication," *IEEE Trans. Wireless Commun.*, vol. 18, no. 8, pp. 4157–4170, 2019.

[5] Y. Liu *et al.*, "Near-field communications: A tutorial review," *IEEE Open J. Commun. Soc.*, vol. 4, pp. 1999–2049, 2023.

[6] C. Feng *et al.*, "Near-field modelling and performance analysis for extremely large-scale IRS communications," *IEEE Trans. Wireless Commun.*, vol. 23, no. 5, pp. 4976–4989, 2024.

[7] H. Lu *et al.*, "A tutorial on near-field xl-mimo communications toward 6g," *IEEE Commun. Surveys Tuts.*, vol. 26, no. 4, pp. 2213–2257, 2024.

[8] ——, "Communicating with extremely large-scale array/surface: Unified modeling and performance analysis," *IEEE Trans. Wireless Commun.*, vol. 21, no. 6, pp. 4039–4053, 2021.

[9] P. Ramezani *et al.*, "Near-field beamforming and multiplexing using extremely large aperture arrays," in *Fundamentals of 6G Communications and Networking*. Springer, 2023, pp. 317–349.

[10] M.-A. Badiu *et al.*, "Communication through a large reflecting surface with phase errors," *IEEE Wireless Commun. Lett.*, vol. 9, no. 2, pp. 184–188, 2020.

[11] S. Zhou *et al.*, "Spectral and energy efficiency of IRS-assisted MISO communication with hardware impairments," *IEEE Wireless Commun. Lett.*, vol. 9, no. 9, pp. 1366–1369, 2020.

[12] Z. Xing *et al.*, "Achievable rate analysis and phase shift optimization on intelligent reflecting surface with hardware impairments," *IEEE Trans. Wireless Commun.*, vol. 20, no. 9, pp. 5514–5530, 2021.

[13] Y. Lu *et al.*, "Performance analysis of RIS-assisted communications with hardware impairments and channel aging," *IEEE Trans. Commun.*, vol. 72, no. 6, pp. 3720–3735, 2024.

[14] R. Sun *et al.*, "Diagnosis of intelligent reflecting surface in millimeter-wave communication systems," *IEEE Trans. Wireless Commun.*, vol. 21, no. 6, pp. 3921–3934, 2021.

[15] H. Taghvaee *et al.*, "Error analysis of programmable metasurfaces for beam steering," *IEEE J. Emerg. Sel. Top. Circuits Syst.*, vol. 10, no. 1, pp. 62–74, 2020.

[16] J. Yang *et al.*, "How practical phase-shift errors affect beamforming of reconfigurable intelligent surface?" *IEEE Trans. Commun.*, vol. 71, no. 10, pp. 6130–6145, 2023.

[17] K. Wang *et al.*, "How long can RIS work effectively: An electronic reliability perspective," in *2023 IEEE 98th Vehicular Technology Conference (VTC2023-Fall)*, 2023, pp. 1–6.

[18] S. Abeywickrama *et al.*, "Intelligent reflecting surface: Practical phase shift model and beamforming optimization," *IEEE Trans. Commun.*, vol. 68, no. 9, pp. 5849–5863, 2020.

[19] C. Ozturk *et al.*, "RIS-aided near-field localization under phase-dependent amplitude variations," *IEEE Trans. Wireless Commun.*, vol. 22, no. 8, pp. 5550–5566, 2023.

[20] M. A. Mosleh *et al.*, "Ergodic capacity analysis of reconfigurable intelligent surface assisted mimo systems with a practical phase shift and amplitude response," *IEEE Trans. Veh. Technol.*, vol. 73, no. 8, pp. 11 441–11 457, 2024.

[21] H. Taghvaee *et al.*, "Fault tolerance in programmable metasurfaces: The beam steering case," in *2019 IEEE International Symposium on Circuits and Systems (ISCAS)*, 2019, pp. 1–5.

[22] X. Pei *et al.*, "RIS-aided wireless communications: Prototyping, adaptive beamforming, and indoor/outdoor field trials," *IEEE Trans. Commun.*, vol. 69, no. 12, pp. 8627–8640, 2021.

[23] W. Tang *et al.*, "Wireless communications with programmable metasurface: Transceiver design and experimental results," *China Commun.*, vol. 16, no. 5, pp. 46–61, 2019.

[24] ——, "Wireless communications with reconfigurable intelligent surface: Path loss modeling and experimental measurement," *IEEE Trans. Wireless Commun.*, vol. 20, no. 1, pp. 421–439, 2021.

[25] ——, "Path loss modeling and measurements for reconfigurable intelligent surfaces in the millimeter-wave frequency band," *IEEE Trans. Commun.*, vol. 70, no. 9, pp. 6259–6276, 2022.

[26] E. Björnson *et al.*, "Intelligent reflecting surface versus decode-and-forward: How large surfaces are needed to beat relaying?" *IEEE Wireless Commun. Lett.*, vol. 9, no. 2, pp. 244–248, 2020.

[27] O. Özdogan *et al.*, "Intelligent reflecting surfaces: Physics, propagation, and pathloss Modeling," *IEEE Wireless Commun. Lett.*, vol. 9, no. 5, pp. 581–585, 2020.

[28] C. Zhang *et al.*, "RIS-Assisted Differential Transmitted Spatial Modulation Design," *Signal Processing*, vol. 230, p. 109767, 2025.

[29] D. Yang *et al.*, "Spatially correlated ris-aided secure massive mimo under csi and hardware imperfections," *IEEE Trans. Wireless Commun.*, vol. 23, no. 9, pp. 11 461–11 475, 2024.

[30] P. Gaenssler *et al.*, "Glivenko–cantelli theorems," in *Encyclopedia of Statistical Sciences*, 2nd ed. John Wiley & Sons, 2006, vol. 5, pp. 1–4.

[31] K. V. Mardia *et al.*, *Directional statistics*. John Wiley & Sons, 2009.

[32] P. Berens, "CircStat: a MATLAB toolbox for circular statistics," *Journal of statistical software*, vol. 31, pp. 1–21, 2009.

[33] D. J. Best *et al.*, "Efficient simulation of the von mises distribution," *Journal of the Royal Statistical Society Series C: Applied Statistics*, vol. 28, no. 2, pp. 152–157, Jun 1979.

[34] E. D. Carvalho *et al.*, "Non-stationarities in extra-large-scale massive mimo," *IEEE Wireless Commun. Mag.*, vol. 27, no. 4, pp. 74–80, 2020.

[35] H. Friis, "A note on a simple transmission formula," *Proceedings of the IRE*, vol. 34, no. 5, pp. 254–256, 1946.

[36] E. Björnson *et al.*, "Power scaling laws and near-field behaviors of massive MIMO and intelligent reflecting surfaces," *IEEE Open J. Commun. Soc.*, vol. 1, pp. 1306–1324, 2020.

[37] C. A. Balanis, *Antenna theory: analysis and design*. John wiley & sons, 2016.

[38] E. Björnson *et al.*, *Introduction to multiple antenna communications and reconfigurable surfaces*. Now Publishers, Inc., 2024.

[39] I. S. Gradshteyn *et al.*, *Table of integrals, series, and products*. Academic press, 2014.

[40] P. Gavriilidis *et al.*, "Active reconfigurable intelligent surfaces: Circuit modeling and reflection amplification optimization," *IEEE Open J. Commun. Soc.*, vol. 6, pp. 5693–5711, 2025.